Photocatalytic approaches for the hydrogen production *via* formic acid decomposition

Miriam Navlani-García[a,b], David Salinas-Torres[a,b], Kohsuke Mori[a,c,*], Yasutaka Kuwahara[a,c], Hiromi Yamashita[a,c*]

[a] Division of Materials and Manufacturing Science, Graduate School of Engineering, Osaka University, 2-1 Yamada-oka, Suita, Osaka 565-0871, Japan

[b] University Materials Institute of Alicante (IUMA), University of Alicante (UA), Ap. 99, Alicante, 03080, Spain

[c] Unit of Elements Strategy Initiative for Catalysts & Batteries (ESICB), Kyoto University, Katsura, Kyoto 615-8520, Japan

ORCID

Miriam Navlani-García: https://orcid.org/0000-0002-6613-2562

David Salinas-Torres: https://orcid.org/0000-0002-1756-5820

Kohsuke Mori: https://orcid.org/0000-0003-3915-4528

Yasutaka Kuwahara: http://orcid.org/0000-0002-5867-6463

Hiromi Yamashita: https://orcid.org/0000-0003-1796-5776

*Corresponding Author: Division of Materials and Manufacturing Science, Graduate School of Engineering, Osaka University, 2-1 Yamada-oka, Suita, Osaka 565-0871 Japan. E-mail address: mori@mat.eng.osaka-u.ac.jp (K. Mori), yamashita@mat.eng.osaka-u.ac.jp (H. Yamashita)

Abstract

The photocatalytic dehydrogenation of formic acid has recently emerged as an outstanding alternative to the traditional thermal catalysts widely applied in this reaction. The utilization of photocatalytic processes for the production of hydrogen is an appealing strategy that perfectly matches with the idea of green and sustainable future energy scenario. However, it sounds easier than it is, and great efforts have been needed to design and develop highly efficient photocatalysts for the production of hydrogen from formic acid. In this work, some of the most representative strategies adopted for this application are reviewed, by paying particular attention to those systems based on TiO_2, CdS and C_3N_4.

1. Introduction

Hydrogen holds great hope in the current energy scenario as a promising energy vector able to replace the widely used vectors based on fossil fuels (coal, oil, and gas). This is not only due to the rapid depletion of fossil fuel reserves, but also due to the increasing energy demand experienced in the last decades and the negative impact of the use of such fuels due to the generation of greenhouse gases [1]. Among greenhouse gases, carbon dioxide (CO_2) is the largest contributor to climate change [2]. As a proof of the impact of the anthropogenic activities in the emission of CO_2, its concentration in the atmosphere has greatly increased since the Industrial Revolution (270–275 ppm in 1750; 310 ppm in 1950; 408 ppm in 2018), with a total emission of 36 Gt CO_2 per year, being 91% of it generated by anthropogenic activities [3].

The worldwide concern about the climate change has resulted in global agreements to combat its tragic consequences, such as the Kyoto Protocol and the more recent Paris Agreement (United Nations Framework Convention on Climate Change; UNFCCC) [4], which aims at keeping global warming below 2 °C. In such energy context, the role of renewable and clean energy is gaining more and more importance. Among them, the use of solar and wind energy as well as hydropower are green energy power sources of interest and they can satisfy the global energy demand. Such renewable sources display advantages as compared to fossil fuels and nuclear-based energy: (i) low variable cost of production; (ii) no production of waste linked to the generation of power; (ii) applicability for decentralized power generation [5].

However, their obvious advantages come with important drawbacks related to their intrinsically dependence on day-night intervals, seasons and fluctuating environmental conditions that result in periods of deficit and surplus of energy output [6, 7]. In such complicated energy scenario, hydrogen, as a never-ending and renewable source of

energy, emerges as an outstanding energy vector for mobile and stationary applications. Hydrogen was recently defined by the International Energy Agency (IEA) as a flexible energy carrier, which can be produced from any energy source, and which can be converted into various energy forms [8].

The widespread implementation of the so-called "hydrogen economy" is not facing only technical barriers, but headwinds related to political and economic interests of using fossil fuels are also underlying causes. However, the scientific community has the moral obligation of searching for possible solutions to solve the issues related to the production, storage, and transportation of hydrogen. The production of hydrogen can be carried out through both renewable and non-renewable sources, but currently steam methane reforming of natural gas is the main process used, which produces approximately 48 % of the total production [9]. However, such process is also linked to the generation of CO_2 emission, which fades the concept of "green hydrogen production" [10]. Aside from that, safety issues related to the physical hydrogen storage by compression and cooling means are also focus of discussion because of the very high pressure level (up to 700 to 800 bar) or very low temperatures (- 252 °C) required [11–15].

The generation of molecular hydrogen (H_2) from hydrogen carrier molecules that contain it in their structure has recently been claimed as an auspicious option. Such molecules provide a unique way to deliver molecular hydrogen in a reversible way by means of chemical reactions and, even though the hydrogen production by these means is not as mature as the classical alternatives, there is already a number of potential candidates that show interesting characteristics [16–25]. Among them, Liquid Organic Hydrogen Carriers (LOHC) are recognized as an ideal option in terms of cost, safety and manageability [26, 27]. Within the LOHC are included all hydrogen storage systems that are liquid in the hydrogen-rich form [11]. Such molecules can be dehydrogenated and re-

4

hydrogenated and show great potential for their use in stationary and transportation applications [5, 28]. Among LOHC investigated for this application (i.e. N-ethylcarbazole, dibenzyltoluene, naphthalene, methanol, toluene, etc. [26, 27]), the suitability of formic acid (HCOOH, FA) is highlighted by the plethora of recent publications reported on the investigation of H_2 production from FA *via* dehydrogenation reaction (HCOOH $\leftrightarrow$ H_2 + CO_2) [29–35]. FA is the simplest carboxylic acid and it has attracted great attention due to its non-toxic character, its stability, and high hydrogen content (4.4 wt.% and 53 g L^{-1}) [30, 31]. Furthermore, FA is readily available from sources such as oxidation of biomass and it is an intermediate, by-product and product of the chemical industry, as well as product of the hydrogenation of CO_2 [36].

The HCOOH/CO_2 system has been claimed to be an ideal environmental-friendly system for the hydrogen storage, so that the CO_2 produced in the dehydrogenation reaction can be re-hydrogenated to HCOOH in a carbon-free emission process [37]. The use of catalysts is vital in the reactions involved in the hydrogen storage and release. Traditionally, the use of homogeneous systems has been used to boost the dehydrogenation of FA, starting with the pioneering investigation reported by Coffey in 1967, in which Pt, Ru and Ir phosphine complexes were used [38]. Even though FA has attracted interest for the H_2 production for more than five decades, its use as a LOHC was not claimed until 2008 by Laurenczy's [39] and Beller's [40] investigations independently [41].

The more convenient use of heterogeneous catalysts has motivated the search for new alternatives to achieve competitive and selective heterogeneous systems able to catalyze the dehydrogenation of FA under mild or moderate conditions. Significant breakthroughs in the field have been achieved while exploring aspects such as the features of the metallic active phase [42–46] or the properties of the support [44, 47–50]. Most of the

investigation reported so far use relatively high temperatures to achieve acceptable conversion of FA into H_2. However, CO can be also produced from FA at high temperatures by following the dehydration reaction ($HCOOH \rightarrow CO + H_2O$), which is a poison of the catalysts used in the fuel cells [51].
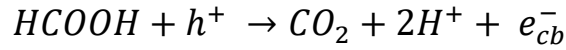
Recently, the photocatalytic dehydrogenation of FA has also attracted great attention as a promising option for the generation of H_2 at room temperature. In most cases, the catalysts used are Mott-Schottky photocatalysts, in which a semiconductor support and metal nanoparticles of diverse composition (i.e. Pd, Pt, Au, Ag, etc.) are used [52].

The utilization of sunlight, as a green and abundant energy source, is of great interest in the current energy scenario. In particular, the use of sunlight for the production of H_2 unites two pillars towards the realization of a sustainable energy future. Most of the solar-to-hydrogen production is based on the water splitting reaction [53, 54], but photocatalytic processes have also been utilized for the production of H_2 from other molecules, such as ethanol [55, 56], methanol [57, 58], glycerol [59, 60], hydrazine [61], ammonia [62, 63], ammonia borane [17, 64–66] etc.
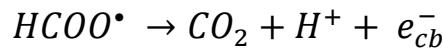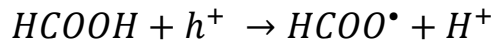
In this manuscript, some of the most representative investigation dealing with the production of H_2 from photocatalytic decomposition of FA are reviewed. The photodecomposition of FA has frequently been investigated from other points of view, such as the degradation of pollutant, the use of FA in photoelectrochemical cells or the role of FA as intermediate in the photocatalytic oxidation of other molecules (i.e. formaldehyde, acetaldehyde, ethanol, and acetic acid) [67, 68]. For that reason, the mechanism involved in the photodecomposition of FA has widely been studied by both experimental and theoretical researchers. However, it remains uncertain because there are various possible adsorption configurations of FA on the surface of the photocatalysts. Ji and Luo reported that FA photodecomposition can take place *via* either one-step

mechanism (without any reaction intermediate) or by two-reaction mechanism [67], in which FA firstly forms a formate radical and it subsequently forms CO_2 with an electron injected in the conduction band of the semiconductor.

- *One-step mechanism*:

$$HCOOH + h^+ \rightarrow CO_2 + 2H^+ + e_{cb}^-$$

- *Two-step mechanism*:

$$HCOOH + h^+ \rightarrow HCOO^\bullet + H^+$$

$$HCOO^\bullet \rightarrow CO_2 + H^+ + e_{cb}^-$$

In order to review the most important breakthroughs achieved in the field, the following sections are divided according to the main component of the photocatalytic system (i.e. TiO_2, CdS, C_3N_4, etc.).

2. Photocatalytic systems based on TiO_2

Starting a review on photocatalytic applications by highlighting the importance of titanium dioxide is a must. Although the investigation of TiO_2 in photocatalysis started long back, it remains one of the most important photocatalytic material because of the great performance showed in multiple applications by virtue of features such as its low cost, chemical inertness, low toxicity, excellent thermal and photo stability, and scalability [69, 70]. The great potential of TiO_2 for a photocatalytic application was firstly discovered by Akira Fujishima in the late 1960s with his investigation on the water photo-splitting [71, 72]. After that, TiO_2 became the most used semiconductor material for photocatalysis and it has been utilized for countless applications [73–77]. Its application for the production of H_2 from FA has also attracted great attention. Some of the strategies found in the literature towards the design of high-performing photocatalysts for the

decomposition of FA using TiO_2 are based on the modification of its properties by means of doping or creating hybrid nanostructure with metal nanoparticles, synthesizing shape-controlled TiO_2 nanoparticles, etc. Such approaches found in the literature are briefly reviewed in the present section.

It is well-known that most of the photocatalytic processes are carried out at room temperature by excluding the heat generated by the infrared part of the solar spectrum by using external cooling systems. In an attempt to fully use the solar energy, both photo and thermal contributions, and maximize therefore the process from an economic viewpoint, Liu and co-workers explored the effect of both energies in the decomposition of FA [78]. For that, Pt/TiO_2 catalysts prepared by photodeposition and with $H_2PtCl_6.6H_2O$ as the metal precursor were used as model to study the photothermal generation of hydrogen up to 90 ºC (i.e. 35, 70, 80, and 90 ºC). The impact of the photo and thermal effects was differentiated by using LED emitting purple, blue and white lights. The sets of catalytic tests consisted in: i) photocatalytic test at 35 ºC (Pt/TiO_2-P); ii) thermal reaction at 90 ºC (Pt/TiO_2-P); iii) photothermal coupling reaction (photo + 35 ºC, photo + 70 ºC, photo + 80 ºC, and photo + 90 ºC, Pt/TiO_2-PT). The obtained results are summarized in Figure 1. As expected, the thermal tests gave higher H_2 yield with the increasing temperature. As for the results achieved with the photothermal experiments, a more pronounced dependence with the temperature was observed and the H_2 yield was 8.1 and 4.2 times than that obtained with the photo and thermal experiments, respectively. Such effect was ascribed to a synergetic effect of the photo and thermal contributions in Pt/TiO_2 catalysts. After performing the test with different LED light irradiations, it was concluded that the H_2 yield followed the order white > blue > purple, confirming the synergistic effect between the thermal catalytic and photocatalytic processes under blue and purple illumination conditions.
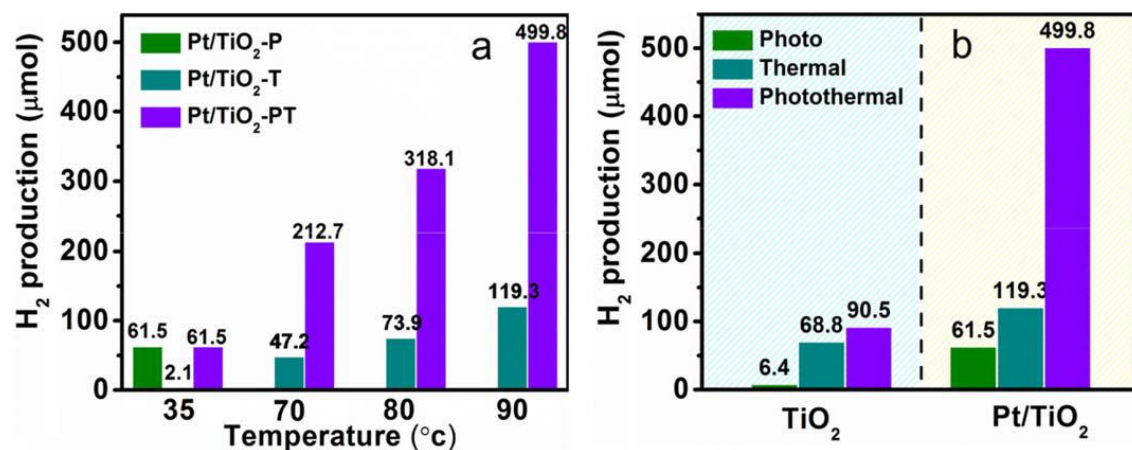
Figure 1. (a) The total amount of H_2 generated in 8 h under photo (35 ºC), thermal (35, 70, 80, and 90 ºC) and photothermal (photo + 35 ºC, photo + 70 ºC, photo + 80 ºC, and photo + 90 ºC) condition over Pt/TiO_2 in the presence of FA (10 vol %); (b) the comparison of 8 h H_2 generation over TiO_2 and Pt/TiO_2 under photo (35 ºC), thermal (90 ºC), and photothermal (photo + 90 ºC) reaction conditions. Reprinted with permission from [78].

The catalysts were deeply characterized, and the tentative mechanism displayed in Figure 2 was proposed. According to what it was found, the photothermal activity was due to the presence of both, non-plasmonic Pt and TiO_2 nanoparticles. According to the proposed mechanism, the production of H_2 mainly takes place on the Pt nanoparticles and the adsorbates derived from FA are the main responsible for the consumption of holes. When the sample is irradiated with UV light, electrons transfer from the valence band to the conduction band and they rapidly transfer to Pt nanoparticles. The adsorbates derived from FA are oxidized by the holes and release hydrogen protons (H^+_f), which are accepted by the water species ($H_2H_fO^+$). Such $H_2H_fO^+$ species diffuse on the surface of the catalyst and exchange the protons with other molecule of water, forming H_3O^+. After that, when H_3O^+ reaches the metal nanoparticles, the electrons go to the LUMO of the molecules adsorbed and H_2 is produced (Figure 2a). On the other hand, the non-plasmonic Pt

9

nanoparticles can use the heat energy creating chemical bond with the adsorbed reactants. Bonding and anti-bonding orbitals of the adsorbed molecules result from the interaction of the molecular orbital of the adsorbed species and the *d* electron states of the nanoparticles (Figure 2b). Then, hydrogen can be formed from FA by the d band electrons of Pt that are excited upon heating. In the case proposed in that study, the irradiation of Pt/TiO$_2$ causes the excitation of the bound electrons of Pt nanoparticles. Such excited electrons inject into the LUMO of the reactants adsorbed to form protons. Upon heating, the excited electrons on the Pt nanoparticles go to higher energy levels, facilitating the activation of the adsorbed reactants and inducing the reaction (Figure 2c).
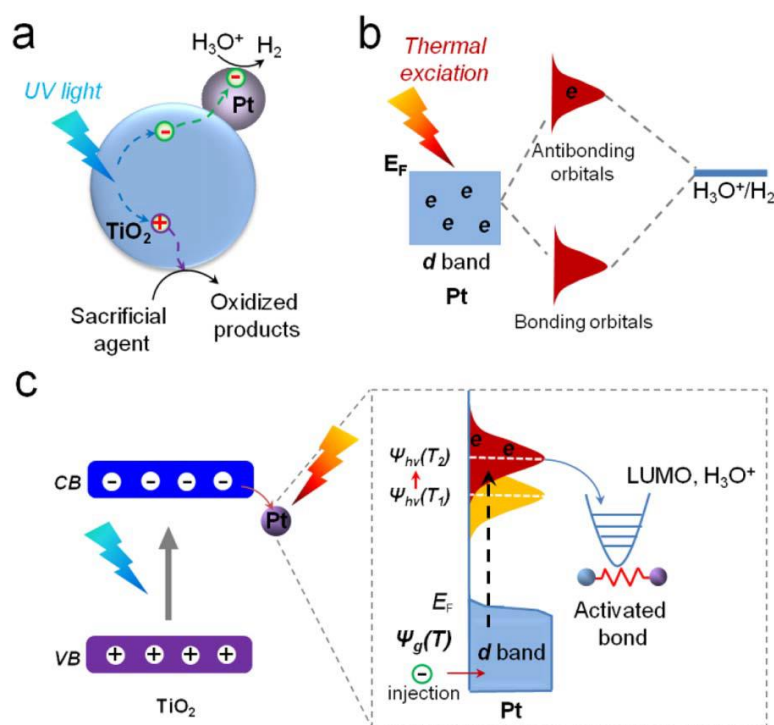

Figure 2. Proposed mechanism of the photothermal catalytic reaction with Pt/TiO$_2$ nanocatalysts. Reprinted with permission from [78].

In line with the investigations reporting on thermal decomposition of FA, in which most of the alternatives used are based on Pd-catalysts, Xiong and co-workers reported

on the photocatalytic decomposition of FA with Pd-TiO$_2$ [79]. In that study, the electronic state of the active site was modified by depositing foreign atoms on Pd-tetrahedron-TiO$_2$. Firstly, the Pd loading was optimizing by checking the activity of catalysts with 5, 10, 18, and 40 wt.% of Pd, being the sample with 18 wt.% the most active. The characterization of the samples indicated that Pd nanocrystals had an average length of 6.3 nm and were covered by {111} facets. The photocatalytic activity in liquid phase was evaluated under various light intensities while collecting the gas generated with a gas burette system (Figure 3).
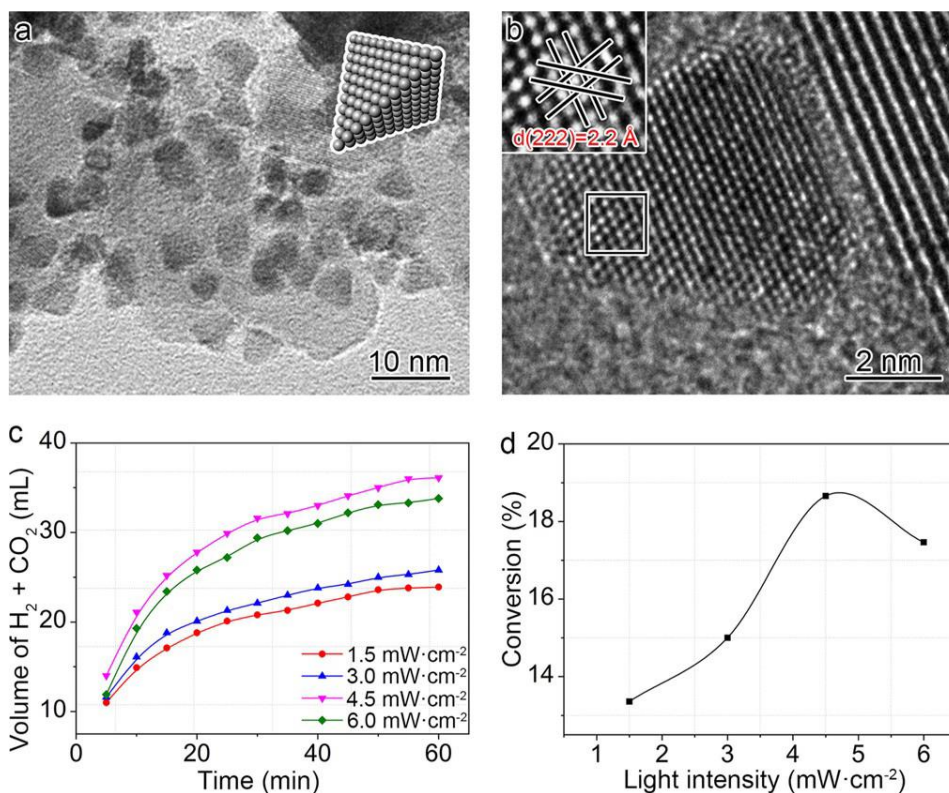

Figure 3. a) TEM and b) HRTEM images of Pd-tetrahedron–TiO$_2$ hybrid nanostructures. c) Volume of H$_2$ and CO$_2$ produced by the decomposition of FA catalyzed by Pd-tetrahedron–TiO$_2$ hybrid nanostructures at different light intensities. d) The dependence of catalytic conversion on light intensity. Conditions: 0.5m aq. HCOOH solution (5 mL), Pd-tetrahedron–TiO$_2$ (Pd:7.74 mg), 90 ℃. Reprinted with permission from [79].

According to the results, it was claimed that the improvement of the activity was ascribed to the increased electron density of Pd by the Mott–Schottky effect. Two effects were considered to explain the photocatalytic tendencies. On the one hand, plasmonic hot electrons generated in Pd particles can inject into the conduction band of TiO_2, which would reduce the electron density of Pd. On the other hand, photoexcitation electrons transfer from TiO_2 to Pd, increasing therefore its electron density. Then, the authors claimed that the photoexcitation of TiO_2 and increase of the electron density on Pd were the main contributions at low light intensities, due to the low plasmonic coefficient of Pd. On the contrary, for higher light intensities (beyond 4.5 mW cm^{-2}), the generation of plasmonic electrons is promoted, while the photoexcitation in TiO_2 is saturated, making the injection of plasmonic electrons from Pd to TiO_2 and the subsequent decrease of the electron density of Pd, the predominant process. After that, foreign metals (i.e. M= Ag^+, Cu^{2+}, Au^{3+} or Pt^{4+}) were deposited on the surface of Pd tetrahedrons so that their surface was partially covered by a layer of PdM alloy. The photocatalytic activity of the resulting samples with a light intensity of 4.5 mW cm^{-2} was assessed. It was observed that the activity in the dehydrogenation of FA was strongly dependent on the foreign metal used. The best performance was achieved with Pd@Ag5%-tetrahedron–TiO_2, with a conversion of 98.7 %, while 63.2 and 35.5 % of conversion was achieved with Cu- and Au-modified Pd-tetrahedron–TiO_2, respectively. Sample modified with Pt displayed a reduced activity. According to the results of DRIFT analysis and the work function of the metals used, such catalytic trend was mainly explained in terms of CO interaction strength and poisoning effect.

Ago et al. also reported on the photocatalytic activity of PdAg-TiO_2 catalysts (AgPd@Pd/TiO_2) [80]. In that case, the desired composition of the metal phase was

achieved by dealloying the AgPd core. Samples with various compositions (i.e. $Ag_{100-x}Pd_x$@Pd/TiO$_2$, with x = 7, 10, 15) were prepared by microwave heating at 100 ℃ during 30 min, 1 h, and 2 h, respectively. The best composition of the catalysts was determined to be $Ag_{93}Pd_7$@Pd/TiO$_2$. Furthermore, the effect of TiO$_2$ was also analyzed by using anatase (A) and P25 (P). The characterization of the catalysts indicated that 0.8 nm-thick Pd shells were achieved on the AgPd cores for both TiO$_2$ supports and the composition, sizes, and morphology did not depend on the TiO$_2$ used. The photocatalytic activity was monitored by measuring the gas generated while irradiating with a Xe lamp and heating at various temperatures (from 27 to 90 ℃). The profiles of the gas evolution with and without illumination are plotted in Figure 4. The analysis of the profiles indicated that the initial reaction rate was improved by a factor of 1.5-1.6 for AgPd@Pd/TiO$_2$ (A) and AgPd@Pd/TiO$_2$ (P) at 27 ℃, respectively, while that factor was 1.1-1.2 at 90 ℃. Such differences observed with the temperature were explained on the basis of the migration of photogenerated electrons from TiO$_2$ to Pd. At low temperatures, the photogenerated electrons transfer from the conduction band of TiO$_2$ to Pd shell with larger work function (5.1, 4.7, and 4.0 eV for Pd, Ag, and TiO$_2$, respectively). The electron-rich Pd species formed upon irradiation were the responsible for the enhancement of the FA decomposition ability. However, for higher temperatures, photogenerated electron have a higher migration rate, but, at the same time, electron–hole pairs recombination is also favored, which eventually resulted in a lower number of electrons reaching the surface of Pd. As for the TiO$_2$ support, it was observed that AgPd@Pd/TiO$_2$ (A) displayed better activity than AgPd@Pd/TiO$_2$ (P) under both light and dark conditions, which was ascribed to the slower electron–hole recombination rate of anatase in comparison to rutile phase present in P25, as well as to its higher specific surface area and strong interaction of anatase phase with AgPd@Pd particles.
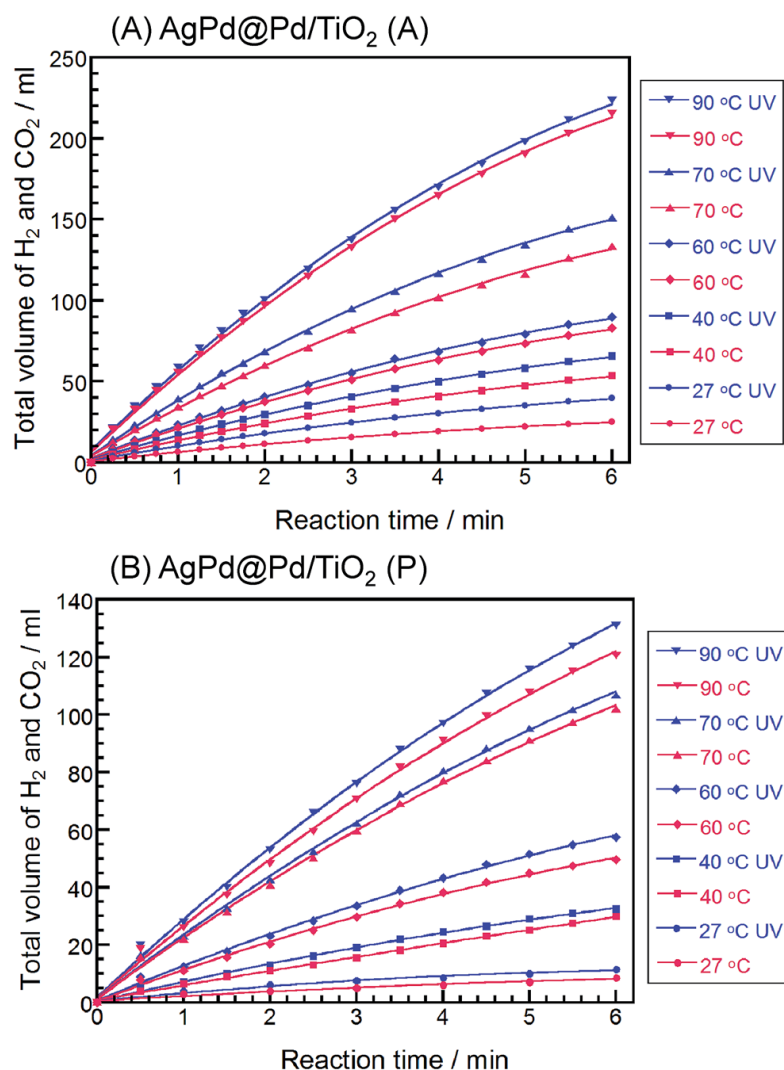
Figure 4. (a) Gas generation by decomposition of FA (0.25 M, 20 mL) vs. time in the presence of (A) AgPd@Pd/TiO$_2$ (A) and (B) AgPd@Pd/TiO$_2$ (P) nanocatalysts at 27–90 ℃ with and without photoirradiation. Reprinted with permission from [80].

Apart from the most commonly investigated PdAg-based catalysts, some other compositions have been studied for this application. For instance, Xue el al. reported on selective photocatalytic decomposition of FA over AuPd nanoparticle-decorated TiO$_2$ nanofibers under simulated sunlight irradiation [81], which were expected to combine the optimum ability of Pd to boost the decomposition of FA with the surface plasmon

resonance (SPR) of Au, as well as the optimized features of the three-dimensional TiO_2 structure. Samples with various Au/Pd ratios were prepared by electrospinning from a solution containing $HAuCl_4$, $Pd(C_2H_3O_2)_2$, tetrabutyl titanate $(Ti(OC_4H_9)_4)$, and poly(vinylpyrrolidone) (PVP). Pd_1/TiO_2 and Au_1/TiO_2 were synthesized as control samples. Among investigated, sample $Au_{0.75}Pd_{0.25}/TiO_2$ displayed the highest H_2 production rate. The presence of alloyed nanoparticles was confirmed by high resolution TEM, XPS, and UV-Vis spectra. Sample with Au nanoparticles showed an absorption band at 590 nm, corresponding to the SPR of Au, while the AuPd-based catalysts displayed a blue-shift to 540 nm with lower intensity due to the increase of electron density in Au particles.

The photocatalytic tests were carried out under simulated sunlight irradiation, with a light intensity of $100 \, mWcm^{-2}$. The results of the photocatalytic test are depicted in Figure 5. The hydrogen generation rate was calculated to be 4.0, 19.5, 54.5, and 88.5 $\mu mol \, h^{-1}$, for TiO_2, Au_1/TiO_2, Pd_1/TiO_2, and $Au_{0.75}Pd_{0.25}/TiO_2$, respectively. Such tendency confirms the ability of Au and Pd to hold the photogenerated electrons from TiO_2 and act as active site for the dehydrogenation reaction. The test under visible light irradiation did not show generation of H_2 for the alloy catalysts, which suggested that TiO_2 excitation is the main responsible for the photocatalytic activity of the sample. Furthermore, the cyclability tests showed a high stability of the alloy photocatalysts during 9 h of reaction. The higher activity displayed by the alloy AuPd-based catalysts was ascribed to the stronger electron-sink effect, that reduced the recombination of electron-hole pairs, which was confirmed by photoelectrochemical tests and photoluminescence measurements. Interestingly, it was demonstrated that the CO poisoned metal surface could be reactivated by means of light excitation of the TiO_2 support upon sunlight irradiation, while such reactivation was not effective under visible light irradiation.
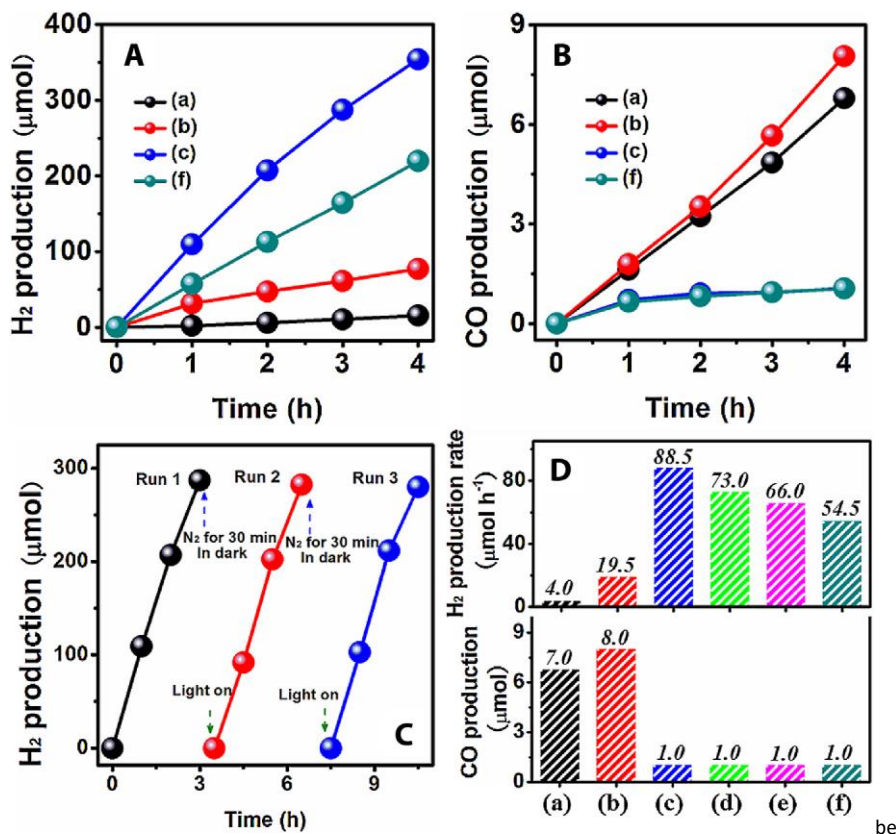
Figure 5. Results of photocatalytic FA decomposition under simulated sunlight irradiation over different nanofibers: (a) TiO_2; (b) Au_1/TiO_2; (c) $Au_{0.75}Pd_{0.25}/TiO_2$; (d) $Au_{0.5}Pd_{0.2}/TiO_2$, (e) $Au_{0.25}Pd_{0.75}/TiO_2$; (f) Pd_1/TiO_2 nanofibers. (A) photocatalytic H_2 production amount versus irradiation time; (B) photocatalytic CO production amount versus irradiation time; (C) cycling test of photocatalytic H_2 production over the $Au_{0.75}Pd_{0.25}/TiO_2$ nanofibers; (D) H_2 production rates and CO production amounts (after 4 h). Reprinted with permission from [81].

Liu et al. also reported on the investigation of Au-TiO_2 photocatalysts [82]. In that study, a more complex visible-light-responsive system formed by Au-La_2O_3/TiO_2 (ALT) hybrid was prepared by a sol-gel method and using different atmospheres (i.e. H_2/CO_2, H_2, CO_2, and N_2; samples denoted as ALT-H_2/CO_2, ALT-H_2, ALT-CO_2, and ALT-N_2, respectively). It was observed that the presence of La inhibited the transformation of

anatase to rutile phase. Furthermore, $La_2O_2CO_3$ was formed upon treatment under H_2/CO_2 atmosphere, which was claimed to be able to decompose to La_2O_3. As for the morphology of the samples, it was observed that Au nanoparticles were embedded in sample ALT-H_2/CO_2 and they were strongly interacting with TiO_2 and La_2O_3 phases and had an average size of 5-6 nm, while larger nanoparticles with hemispherical shape were identified in sample ALT-H_2. The presence of $La_2O_2CO_3$ in samples treated under H_2/CO_2 atmosphere and its dynamic formation and decomposition was found to be responsible for the good dispersion of the nanoparticles observed in ALT-H_2/CO_2. However, Au nanoparticles were not detected in ALT-CO_2 and ALT-N_2, possible due to the absence of reducing agent in the calcination step. UV-vis characterization of the catalysts revealed that co-doping of La and Au provoked a reduction of the band gap, following the order ALT-H_2 (2.56 eV) < ALT-H_2/CO_2 (2.66 eV) < ALT-CO_2 (2.77 eV) < ALT-N_2 (2.84 eV), which was ascribed to a synergistic effect between Au and La under the different atmospheres used. In addition, photoluminescence analysis demonstrated the prolonged lifetime of electron-hole pairs in sample ALT-H_2/CO_2. As expected after all the results of characterization of the samples, ALT-H_2/CO_2 displayed the best photocatalytic performance among investigated, with a H_2 production rate of 178.4 μmol g_{cat}^{-1} h^{-1}, which was much higher than those rates achieved with the catalysts prepared under the other atmospheres under study. A plausible mechanism for the decomposition of FA was proposed, which is schematized in Figure 6. The photon absorbed by La-doped TiO_2 excite photogenerated electrons to the conduction band and generate holes in the valence band. Firstly, electrons are transferred to Au nanoparticles promoting the decomposition of HCOOH into $HCOO^-$ and H^+. H^+ can produce H_2 by reduction with an electron, and $HCOO^-$ reacts with a photogenerated hole in TiO_2 forming a free radical ($HCOO^{\cdot}$). Subsequently, $HCOO^{\cdot}$ is oxidized by holes and produces CO_2 by releasing a H^+. In the

mechanism proposed, $La_2O_2CO_3$ plays a vital role in promoting the decomposition of FA and the desorption of CO_2 from the surface of the catalyst.

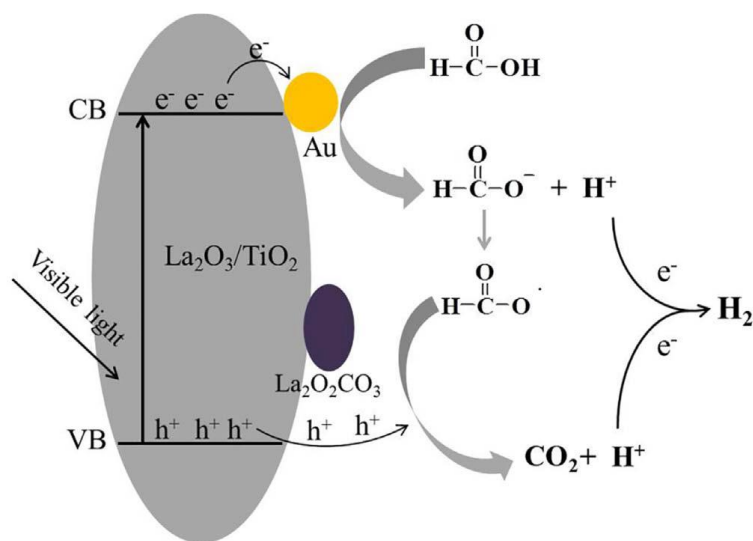**Figure 6.** Schematic illustration for the reaction mechanism of photocatalytic decomposition over ALT-H_2/CO_2 photocatalyst. Reprinted with permission from [82].

As for noble-metal-free photocatalysts, some nice works can also be found in the literature. For instance, Andreozzi et al. reported on novel nano-TiO_2 photocatalytic system based on the solar reforming of FA in presence of cupric ions and chlorides, in a study in which the effect of the pH values, initial concentration of FA, chloride and cupric ion in the H_2 production ability was investigated. The H_2 production was suggested to proceed *via* the following steps:

- *Step 1*: reduction of cupric ions to cuprous with a simultaneous oxidation of formic acid.

$$Cu(II) \xrightarrow{e^-_{CB}} Cu(I) \xrightarrow{e^-_{CB}} Cu(0)$$

$$HCOOH \xrightarrow{h^+_{VB}} CO_2^{\bullet-} + 2H^+$$
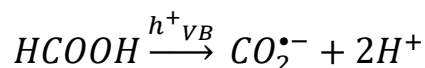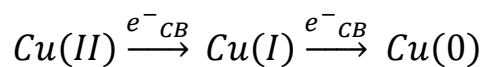
- *Step 2*: photolysis of some chloride complexes of cuprous ions.

$$CuCl_2^- + H^+ \xrightarrow{h\nu} Cu^{2+} + 2Cl^- + e_s^-$$

$$CuCl_3^{2-} + H^+ \xrightarrow{h\nu} Cu^{2+} + 3Cl^- + e_s^-$$
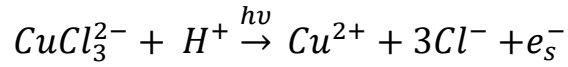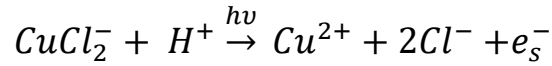
Dong et al. investigated on the engineering of binary CuO/TiO_2 heterojunction nanofibers prepared from electrospinning and followed calcination treatment [83]. It was found that after irradiation for 30 min during the photodecomposition of FA, the binary heteroconjunction (CuO/TiO_2) changed to a heteroconjunction formed by four components ($Cu/Cu_2O/CuO/TiO_2$) originated by a photo-assisted recrystallization reaction (Figure 7), enhancing the separation of electron and hole pairs. Such aspect is crucial, because the production of H_2 takes place in two steps photoreaction, the generation of H^+ *via* photocatalytic oxidation of HCOOH by the holes in the valence band, and the formation of H_2 *via* photocatalytic reduction of H^+ with the photoinduced electrons in the conduction band. Then, as the oxidation reaction by the holes occurs before the reduction, the lifetime of the electrons should be longer than that of the holes. In this particular case, HCOOH can be oxidized to H^+ by the holes accumulated in the valence band of CuO, because of their higher potential ($\sim$ +2.05 V) than those of the pair CO_2/HCOOH ($\sim$ −0.61 V). However, the position of the conduction band of CuO is below the reduction potential of the pair H^+/H_2 ($\sim$ +0.36 V and $\sim$ -0.42 V, respectively), meaning that the reduction of H^+ to H_2 by the photoinduced electrons is not thermodynamically favored. For that reason, Cu_2O and Cu species are formed from the reduction of CuO, species that are visible-light responsive and inexpensive co-catalysts, respectively. As a result, the quaternary multi-heterojunction photocatalysts ($Cu/Cu_2O/CuO/TiO_2$) displayed 40 times higher production of H_2 from FA than pure TiO_2 nanofibers counterpart.
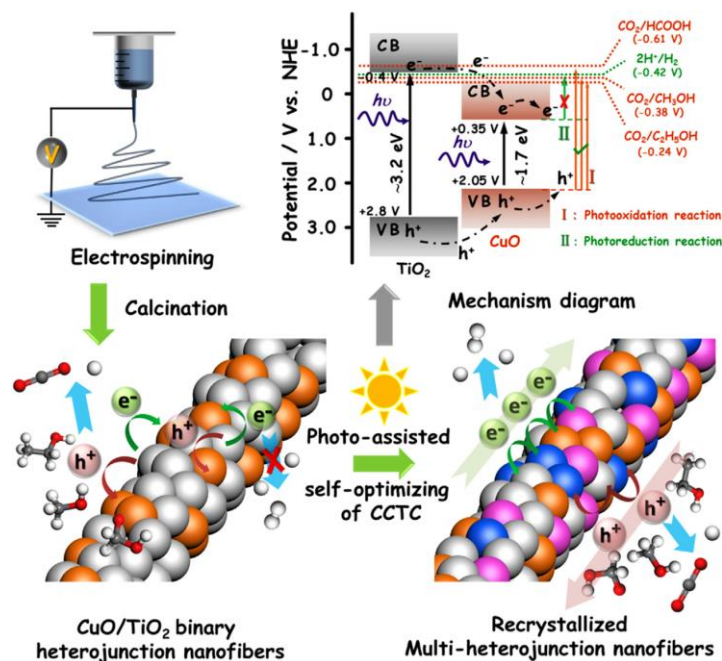
Figure 7. Schematic diagrams for the synthesis route of CuO/TiO$_2$ binary heterojunction nanofibers and the photo-assisted self-optimizing of charge-carriers transport channel (CCTC) through a recrystallization process during the photocatalytic decomposition of organic hydrogen-carrier molecules. Reprinted with permission from [83].

3. Photocatalytic systems based on CdS

The previous section mentioned some benefits of TiO$_2$ in photocatalytic reactions and summarized some examples of TiO$_2$-based catalysts for the FA decomposition. However, their limitation in the visible-light range creates the necessity of searching for photocatalysts with wider light responsive range. In this sense, metal sulphides have extensively been studied because they exhibit an important visible-light response although their efficiency is poor. As mentioned before, the recombination between electron and hole is related to the efficiency. An approach to limit such recombination is the use of photocatalysts with a high CB position, which present an interesting reduction capability. At this point, CdS (with a band gap of ~ 2.5 eV) is an interesting option that has attracted much attention due to its wide visible-light range together with its simple

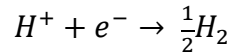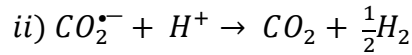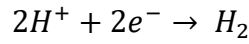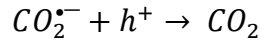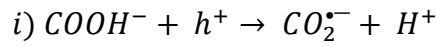synthesis and low cost. Furthermore, it fulfils the thermodynamic aspects of some of the most studied photocatalytic reactions [84, 85]. Regarding the photocatalytic decomposition of FA, a few studies on CdS-based photocatalysts have also been reported until now. In 1968, Willner and Goren reported on semiconductor CdS particles for the generation of H_2 from the FA decomposition [86]. In this particular case, they used both formate solution and deuterated counterpart to evaluate the photodecomposition to produce H_2. The yield of H_2 was higher than 90 % for the formate solution while the deuterated solution displayed a lower H_2 evolution rate, indicating that the limiting step of the formate oxidation reaction was the generation of holes in CdS particles (h^+ + $HCO_2^- \rightarrow CO_2^{\bullet-}$ + H^+) and that water was the source of H^+ for the H_2 formation. Moreover, they realized that the formation of $CO_2^{\bullet-}$ (reducing agent) after the photodecomposition promoted the presence of Cd metal in the system. Nedoluzhko et al. also reported that Cd^0 was involved in the photoformation of H_2 [87]. In that study, a solution of CdS particles ($\sim$1.5 µm), formate and buffer was irradiated under anaerobic conditions. Among evolved gases, H_2 profile exhibited an induction time and then, the rate of H_2 evolution increased rapidly. This turning point was related to the generation of Cd^0 from CdS. The formation of cadmium (metallic state) was firstly attributed to the presence of formate and they proposed that two $CO_2^{\bullet-}$ anion radicals, which acted as reducing agents, are involved in the reduction process of CdS.

$$CdS + 2CO_2^{\bullet-} \rightarrow Cd^0 + S^{2-} + 2CO_2$$
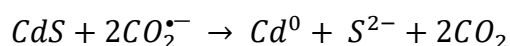
During this process, electrons present in the conduction band reduced water to form H_2. However, they noticed that H_2 gas evolution did not happen at the beginning of the photoreaction and they claimed that one equivalent of $CO_2^{\bullet-}$ participated to reduce the lattice Cd^{2+}. Therefore, the proposed mechanism consisted of a trapping of electrons, followed by a reduction.

$$CdS + e_{cb}^- \rightarrow (Cd^{2+}e^-S^{2-})$$

$$(Cd^{2+}e^-S^{2-}) + CO_2^{\bullet-} \rightarrow Cd^0 + CO_2 + S^{2-}$$
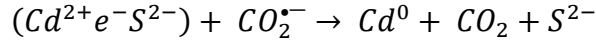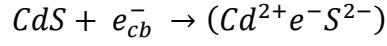
According to the standard reduction potential values, it was stated that electrons of CdS conduction band could not reduce the lattice Cd^{2+} to Cd^0. Once a determined amount of the lattice Cd^{2+} was converted to Cd^0, the H_2 gas evolution commenced following the suggested pathways.

$$i)\ COOH^- + h^+ \rightarrow CO_2^{\bullet-} + H^+$$
$$CO_2^{\bullet-} + h^+ \rightarrow CO_2$$
$$2H^+ + 2e^- \rightarrow H_2$$

$$ii)\ CO_2^{\bullet-} + H^+ \rightarrow CO_2 + \tfrac{1}{2}H_2$$
$$H^+ + e^- \rightarrow \tfrac{1}{2}H_2$$

Although CdS exhibited photocatalytic activity towards the FA decomposition, it was restricted for CdS in powder form. For instance, Nedoluzhko et al. also observed that the formation of Cd^0, which played a pivotal role in the H_2 formation from FA decomposition, depended on a limited amount of Cd^{2+}. Therefore, different strategies based on CdS have been explored to enhance the photocatalytic activity in the FA decomposition. Chen et al. reported that CdS particles were embedded on titanate nanotubes (TNTs) using a hydrothermal synthesis [88]. From TEM images, confined CdS particles as well as CdS particles suported on the surface of TNTs were observed. Morevoer, XRD patterns and UV spectra confirmed the presence of CdS particles. The photocatalytic activity towards the H_2 production was evaluated in a 10 vol % FA solution. CdS/TNTs produced 179.4 µmol of H_2 after 3 h while TNTs only generated 0.09 µmol. This enhancement could be related to the transfer of photogenerated electrons from the valence band to the conduction

band. These electrons could be transferred to TNTs because both valence band and conduction band positions of CdS are higher compared to TNTs. Recently, Liou et al. published a composite that consisted of Pt, CdS, and TNTs synthesized by microwave hydrothermal method [89]. The H_2 evolution rate for different catalysts were assessed in an aqueous FA solution (10 vol %) under visible light. Both TiO_2 and TNTs catalysts did not displayed activity towards the FA decomposition. However, the addition of CdS into titania structures promoted the photocatalytic activity, being more active in the case of Cds/TNTs (295.0 µmol h^{-1}) than CdS/TiO_2 (118.7 µmol h^{-1}). Such effect was attributted to a higher active surface area for TNTs compared to TiO_2, which boosted the adsorption of FA onto the active sites and reduced the recombination of electron-hole pair. After this, Pt was loaded on titania-based photocatalyst in order to trap the photogenerated electrons, resulting in photocatalysts more active towards the FA decomposition. To do that, impregnation and photodeposition methods were carried out, leading to Pt-CdS/TNT samples prepared by the thermal impregnation method with different Pt loadings, which exhibited worst photocatalytic activities compared to that of CdS/TNT photocatalyst. This decline in the H_2 production was related to the agglomeration after the thermal impregnation. However, Pt-CdS/TNT synthesized by photodeposition of Pt displayed a remarkable photocatalytic activity for the H_2 production (661.1 µmol h^{-1}). The enhancement of the H_2 production was due to a smaller Pt nanoparticle size and a well-distribution of nanoparticles onto CdS/TNT, resulting in a better contact between Pt and TNTs that improved the separation of electron-hole pair. Concerning the mechanism, it was suggested that the photogenerated electrons were transferred from the valence band to the conduction band of CdS, and therefore the concentracion of holes increased in the valence band. According to the band gap of TNTs, the photoelectrons in CdS jumped quickly into TNTs. Moreover, it was indicated that Ti^{3+} species present in TNTs (due to

the oxygen vacancy) may capture electrons and Pt nanoparticles act as active sites for the H_2 production. Additionally, Ti^{4+} species was suggested as a hole cocatalyst because the photogenerated holes in the CdS surface can be trapped by Ti^{4+} species, avoiding the CdS photocorrosion.

A different strategy was tackled by Li et al. who reported on the use of visible light-driven photocatalyst based on a CdS-ZnS composite with heterogeneous structure [90]. In such system, CdS, with a narrow band gap and highly photo-sensitivity, showed great reactivity for the production of H_2, while ZnS, with a wider band gap, reduced the recombination of electron-holes pairs. The nanoparticles of the CdS-ZnS photocatalyst were prepared by a microemulsion technique in a system composed of water/Triton X-100/1-butanol/n-hexane, and using $Cd(NO_3)_2$, $Zn(NO_3)_2$, and $Na_2S.xH_2O$, as precursors of Cd, Zn and S^{2-}, respectively. The heterogeneous solid formed was composed by ZnS deposited on the surface of crystals of CdS. The obtained photocatalysts were evaluated in the production of H_2 and it was shown that only 13.7 µmol h^{-1} of H_2 was generated from CdS, while 189.5 µmol h^{-1} was produced from the CdS-ZnS and no H_2 was detected using bare ZnS. The enhancement observed for the heterogeneous CdS-ZnS system was claimed to be due to the suppression of electron-hole pairs recombination due to the presence of ZnS, which makes electrons available for the evolution of H_2. It was proved that, aside from that effect, the addition of ZnS was responsible for the good stability against photo-corrosion displayed by CdS-ZnS. Moreover, it was observed that the ZnS coating avoided the Cd^{2+} leaching from the photocatalysts, which also helped to maintain the reactivity of the samples (Figure 8).
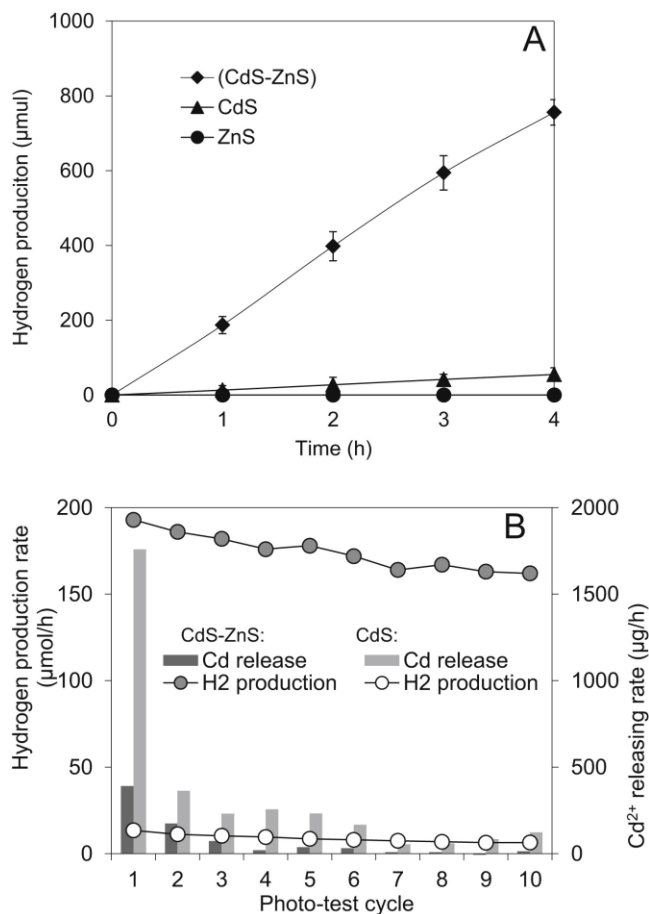
Figure 8. A) Hydrogen production in the formic acid solution (10%) by the composite CdS-ZnS, bare CdS and bare ZnS, under visible light; and (B) stability of CdS-ZnS and bare CdS in terms of the hydrogen production rate and leaching of Cd^{2+} from the catalysts during the repeated photocatalytic tests (at least 4 h for each test cycle). Reprinted with permission from [90].

Following with the heterogeneous systems based on CdS, Xu et al. reported on multi-core–shell CdS@ZIF-8 structures prepared by a two-step method [91]. In the synthetic protocol used in that study, polyvinylpyrrolidone (PVP) was used to stabilize the nanoparticles of CdS and ZIF-8 shells with controlled thickness (from 13.6 to 102 nm) were formed on the surface of CdS. The photocatalytic performance evidenced the superiority of the core-shell structure compared to bare CdS nanoparticles. It was observed that core–shell structures showed better selectivity towards the production of H_2 *via* FA dehydrogenation reaction.

Zhang et al. reported on the preparation of composite of aluminium-substituted mesoporous silica (Al-HMS) molecular sieve coupled with CdS (CdS/Al-HMS) [92]. It was observed that the addition of Ru enhanced the photocatalytic activity as a consequence of the separation of photogenerated charge-carrier. Among investigated, sample 0.07Ru/CdS/Al-HMS exhibited the highest H_2 evolution activity (3.7 mL h^{-1}).

Reisner et al. investigated on a CdS-based photocatalyst that efficiently converted FA into H_2 or CO by boosting the dehydrogenation or dehydration reaction, respectively, by means of controlling the selectivity of the reaction by using 3-mercaptopro-pionic acid (MPA) as a capping ligand (QD-MPA) [93]. Under visible-light irradiation, 52.1 mmol H_2 $g_{cat}^{-1}h^{-1}$ were generated with QD-MPA, which was enhanced by the addition of Co (QD-MPA/$CoCl_2$; 116 mmol H_2 $g_{cat}^{-1}h^{-1}$). However, 218 H_2 $g_{cat}^{-1}h^{-1}$ were achieved upon utilization of full solar spectrum. Aside from the effect of Co species in boosting the catalytic performance, it was also proved in that study that the selectivity of the FA decomposition towards either H_2 or CO could be modified by means of modifying the surface of CdS with ligands, such as $[Me_3O]BF_4$.

Piao et al. reported on the use of ultrasmall cobalt phosphide nanoparticle (CoP) as efficient cocatalysts for photocatalytic dehydrogenation of FA [94], in a study in which a CdS/CoP@RGO hybrid was evaluated. In order to obtain the final catalysts, Co_3O_4@SiO_2 nanospheres were firstly prepared using a microemulsion method and subsequently decorated by polyethyleneimine (PEI) and loaded on graphene oxide (GO). After that, SiO_2 was removed to obtain Co_3O_4 dispersed on RGO and the final CdS/CoP@RGO photocatalyst was prepared by phosphidation and loading CdS nanoparticles by ultrasonic treatment. The performance of CoP was assessed by comparison with the counterpart noble-metal based catalysts (CdS/Pt@RGO, CdS/Pd@RGO, CdS/Au@RGO, and CdS/Ru@RGO). It was shown that the TOF values

were 196, 244, 106, 107, and 63 h^{-1}, for CoP, Pt, Pd, Au, and Ru, respectively, which evidenced the promising behaviour of CoP as a cocatalyst for the photocatalytic dehydrogenation of FA. Following with the non-noble-free photocatalysts, Khan et al. reported a system based on Ni and Co loaded on CdS nanorods (NRs), that were synthetized *via* controlled thermolysis of cadmium (II) bis(dibutylcarbamodithioate) in ethylenediamine [95]. Using such system and due to the redox potentials of Ni and Co in relation to the band positions of CdS NRs, electron and holes were shuttled from CdS to Ni and $CoCl_2$ species, respectively, which led to higher stability and photocatalytic performance. The evaluation of the catalytic performance under visible-light irradiation revealed that the H_2 production ability followed the order CdS < Co/CdS < Ni/CdS < Co-Ni/CdS.

4. Photocatalytic systems based on C_3N_4

Graphitic carbon nitride (g-C_3N_4), a polymeric semiconductor, has elicited great attention in the context of the search for robust and visible-light-active semiconductor photocatalysts. It is formed by ordered tri-s-triazine subunits connected through planar tertiary amino groups within a layer and weak van der Waals force between layers. It shows appealing electronic properties, high physicochemical stability, and easy synthesis from N-containing precursors (i.e. urea, cyanamide, dicyandiamide, melamine, etc.). It has a moderate band gap (2.4 - 2.8 eV) that results in an onset visible light absorption of ~ 450 nm [96, 97]. Even though the history of C_3N_4-based polymer started in the nineteenth century by the investigation of Berzelius and Liebig [98], its use in heterogeneous catalysis started much later in 2006 [99] and its properties as a metal-free conjugated semiconductor photocatalysts for the evolution of H_2 was pioneering reported by Wang just 10 years ago [100].

Since then, g-C_3N_4 has widely been utilized in numerous photocatalytic applications, such as water splitting, CO_2 reduction, and degradation of pollutants, etc. [101] [102, 103]. Recently, g-C_3N_4 has also received attention as a catalyst for the H_2 production from hydrogen carrier molecules [44, 50, 64, 104]. In the case of g-C_3N_4-photocatalysts used for the decomposition of FA, they contain metal nanoparticles so as to construct Mott–Schottky photocatalysts, in which the charge separation is enhanced. This was the case of the study reported by Chen et al. [105]. In that investigation, Mott–Schottky type Pd-C_3N_4 photocatalysts, with mesoporous C_3N_4 (mpg-C_3N_4) as support, were prepared by wet impregnation and the resulting material was denoted as Pd@CN. For that, mpg-C_3N_4 was firstly synthetized from cyanamide and a Ludox HS40 solution, and subsequently impregnated with $PdCl_2$ to have a final metal loading of 8 %. Furthermore, reference samples with N-doped layered carbon and carbon black (Pd@N-LC and Pd@CB, respectively) were also synthetized. The average nanoparticle size was determined to be of 3-5 nm for Pd@CN and Pd@N-LC, and 10 nm for Pd@CB. In order to assess the performance of the samples, catalytic and photocatalytic tests were monitored. It was observed that, in dark conditions (i.e. catalytic test at 15 ºC), Pd@CN displayed the highest TOF number among investigated (49.8 mol H_2 $mol^{-1}Pd$ h^{-1}), which was attributed to the Mott–Schottky effect (i.e. support effect). Such effect was confirmed by the decreased intensity of the photoluminescence spectra after the loading of Pd nanoparticles on mpg-C_3N_4. In addition, it was found that such good catalytic activity was further increased upon visible-light irradiation (71.0 mol H_2 $mol^{-1}Pd$ h^{-1}). It was claimed that the enhancement observed in the catalytic activity under light irradiation conditions was due to the electron enrichment of Pd nanoparticles, which in turn was strongly dependent on the wavelength of the light used (See Figure 9).
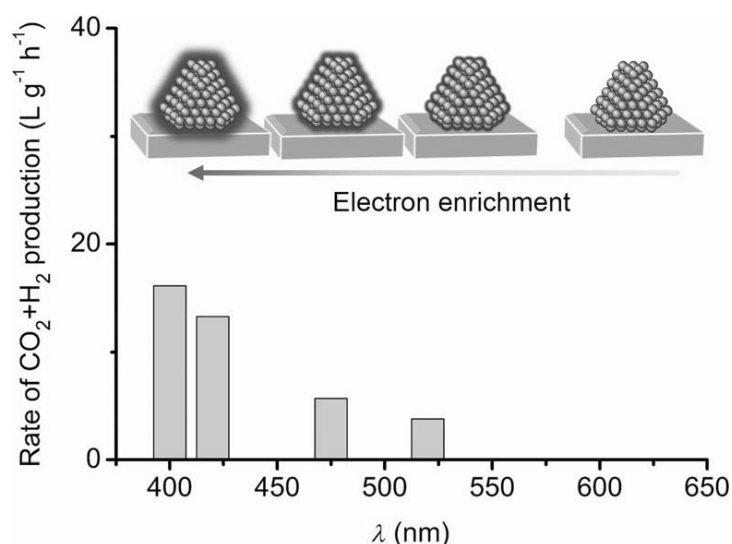
Figure 9. Dependence of the activity of Pd@CN on the irradiation wavelength for the photocatalytic decomposition of FA. Reaction conditions: 1m aqueous FA solution (10 mL), Pd@CN-1% (20 mg),1 h, 15 °C. Reprinted with permission from [105].

Yu et al. also reported on the application of Mott–Schottky heterojunctions [106]. In that case, PdAg nanowires (NWs) with various Pd/Ag compositions (Pd_7Ag_3 NWs@g-C_3N_4, Pd_5Ag_5 NWs@g-C_3N_4, Pd_3Ag_7 NWs@g-C_3N_4, and Pd NWs@g-C_3N_4) were *in-situ* formed on g-C_3N_4. XPS analysis confirmed the electron transfer from Ag and *g*-C_3N_4 to Pd of the Pd_5Ag_5 NWs@*g*-C_3N_4 Mott–Schottky heterojunction, creating electron-rich Pd species that are favorable for facilitating the O–H cleavage and strengthening the adsorption of formate. On its side, the support serves as a proton scavenger for the dissociation of O-H, forming protonated *g*-C_3N_4, which facilitates the production of H_2 and CO_2 *via β*-hydride elimination of Pd-formate. The catalytic activity displayed dependence with the composition of the nanoparticles, with initial TOF of 346, 420, 242, and 105 h^{-1}, Pd_7Ag_3 NWs@*g*-C_3N_4, Pd_5Ag_5 NWs@*g*-C_3N_4, Pd_3Ag_7 NWs@*g*-C_3N_4 and Pd NWs@*g*-C_3N_4, respectively. Furthermore, the performance of some control samples was also assessed to point out the effect of the Mott–Schottky heterojunction. The effect of the visible-light intensity on the photocatalytic activity of Pd_5Ag_5 NWs@*g*-C_3N_4 was

29

also investigated, which showed and increasing dehydrogenation rate with the light intensity.

Stucky et al. also investigated on AgPd nanocatalysts supported on g-C_3N_4 (denoted as AgPd/CN) [104]. In that case, microsized mesoporous carbon nitride hollow spheres were synthetized from melamine-cyanuric acid network, and subsequently impregnated with K_2PdCl_4 and $AgNO_3$. As indicated by the characterization results, the resulting nanoparticles had an average size of 7.5 ± 1.0 nm and a Ag/Pd ratio of 1/1. The comparison with reference samples prepared from SiO_2 and activated carbon demonstrated the vital role of the N-functional groups in C_3N_4 in achieving highly dispersed alloy AgPd nanoparticles. The electron density enrichment of Pd species *via* electron donation from C_3N_4 and Ag to Pd was also demonstrated by XPS analysis. It was also claimed that the electron density of Pd could be further increased by the photoexcited electron transfer from the semiconductor support, which in turn would suppress the electron-hole pairs recombination. As a consequence of the resulting unique electronic features, AgPd/CN displayed much higher activities than Ag/CN and Pd/CN counterpart, which was further enhanced under visible-light irradiation. H/D isotope experiments were also followed using D_2O to investigate the contribution of the semiconductor and the direction of the charge carrier in the components of the photocatalysts. The results of the relative atomic amount and atomic ratio of H and D in the gas produced from FA decomposition at 30 ºC is depicted in Figure 10.
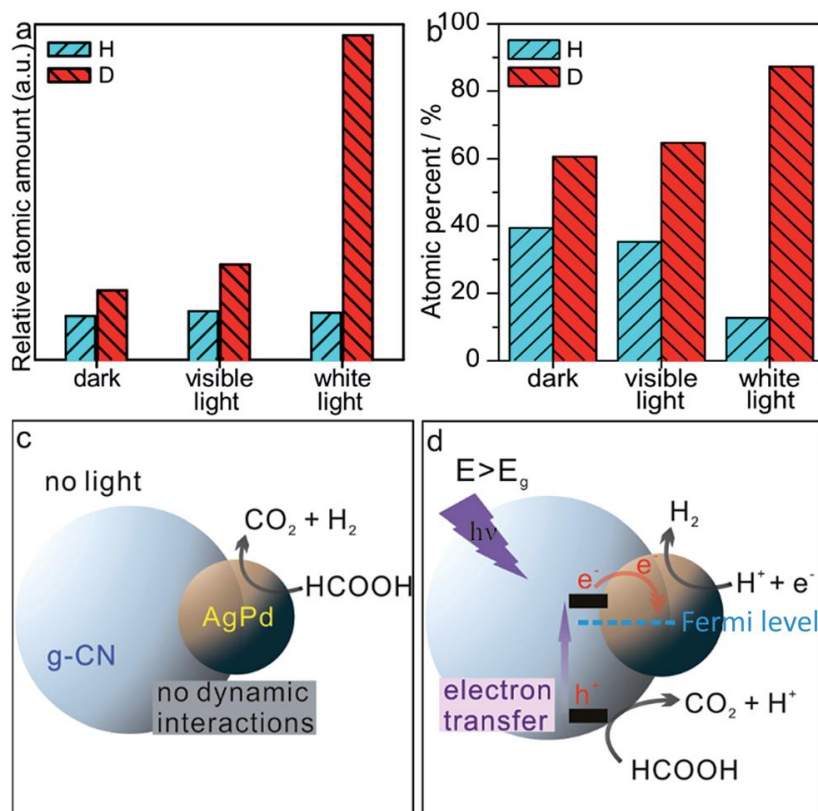
Figure 10. (a, b) Kinetic isotope effects for FA decomposition with the AgPd/CN-3% catalyst in D_2O at 30 °C under different conditions; (a) the relative atomic amount and (b) the atomic ratio of deuterium/hydrogen to the total amount of hydrogen and deuterium is shown. The reaction pathway and mechanism for (c) catalytic route under dark or (d) photoelectrochemical route under light with incident energy higher than bandgap of CN. Reprinted with permission with [104].

It was observed that the atomic percentage of D under visible-light was slightly higher than that under dark conditions (64.7 and 60.6 %, respectively), while it increased to 87.3 under UV-light, indicating that the photocatalytic activity was wavelength-dependent. Under UV-light, the energy of the photon is able to excite the electron-hole pair directly and the water splitting occurs in the different components of the catalysts (i.e. photocathode: AgPd for reduction of water; photoanode: C_3N_4 for the oxidation of FA), so that FA serves as the electron donor and D_2O acts as the electron acceptor. The higher

content of D observed in the gas product demonstrated that D_2O is the source of D, due to the photoelectrochemistry with half reaction separated. However, for very short wavelength, FA photolysis to CO can take place.

Following with the Mott-Schottky photocatalysts, Liu et al. recently reported on the application of plasmonic AuPd alloy nanoparticles supported on super small carbon nitride nanospheres (Au_xPd_y/CNS) for the H_2 production [52]. The catalysts were designed so that Au could capture the irradiation energy, which results in electron with high density on its surface by the LSPR effect. Such high energy electrons can migrate to Pd active sites and results in enhanced photocatalytic performances. For the preparation of the catalysts, carbon nitride nanospheres were firstly synthetized from cyanamide and using SiO_2 as a template. They were subsequently impregnated with $HAuCl_4$ and H_2PdCl_4 with various mole ratio (i.e. 1:0, 2:1, 1:1, 1:2, and 0:1) to achieve different compositions of the alloy nanoparticles. The resulting photocatalysts were denoted as Au/CNS, Au_2Pd_1/CNS, AuPd/CNS, Au_1Pd_2/CNS and Pd/CNS, respectively, according to the composition of the nanoparticles. A sample prepared from bulk C_3N_4 (AuPd/Bulk CN) was also prepared as a reference material. TEM analysis revealed that the average size of g-C_3N_4 nanospheres and AuPd nanoparticles was 20 and 3 nm, respectively. Once again, the fine distribution of AuPd nanoparticles on the nanospheres was attributed to the anchoring effect of the uncondensed amine groups on the surface g-C_3N_4. XPS analysis confirmed the strong interaction and distribution of charge from Au to Pd in the AuPd nanoparticles, as well as the electron donation from the support to Pd species. As for the catalytic results (See Figure 11), in was observed that, under dark conditions, the generation of gas was equal to 86, 137 and 171 mL for Pd/CNS, AuPd/Bulk CN, and AuPd/CNS, respectively, confirming the beneficial effect of the alloyed nanoparticles. All Pd-containing showed improved activity under visible-light as compared to that under

dark conditions, being more marked in sample AuPd/CNS, with displayed the highest activity (TOF value of 1017.8 h^{-1}). Such enhancement was attributed to the donation of electron from CNS to the nanoparticles due to the Mott-Schottky effect as well as to the alloying and plasmonic effects that lead to the redistribution of charge under visible-light irradiation. The contribution of alloying and plasmonic effects was confirmed by assessing the performance of samples with various composition of the alloy nanoparticles (Au_2Pd_1/CNS, AuPd/CNS, Au_1Pd_2/CNS, and Au_1Pd_2/CNS) and the physically mixed counterpart catalysts (Au_2+Pd_1/CNS, $Au+Pd$/CNS, and Au_1+Pd_2/CNS).

Considering that Pd is the active phase, a decrease of the activity with increasing the Au content could be expected. However, the positive alloying and plasmonic effect was confirmed by the enhancement achieved by the AuPd-based catalysts. Samples Au+Pd/CNS and AuPd/CNS, displayed the best performances among physically mixed and alloy catalysts, respectively. The comparison between Pd/CNS and Au+Pd/CNS revealed an increasing rate of 24.8 %, which corresponds to the plasmonic effect. The increasing rate in the case of the alloy catalysts was of 143.2 %, indicating that the alloy effect is much more important than the plasmonic effect.
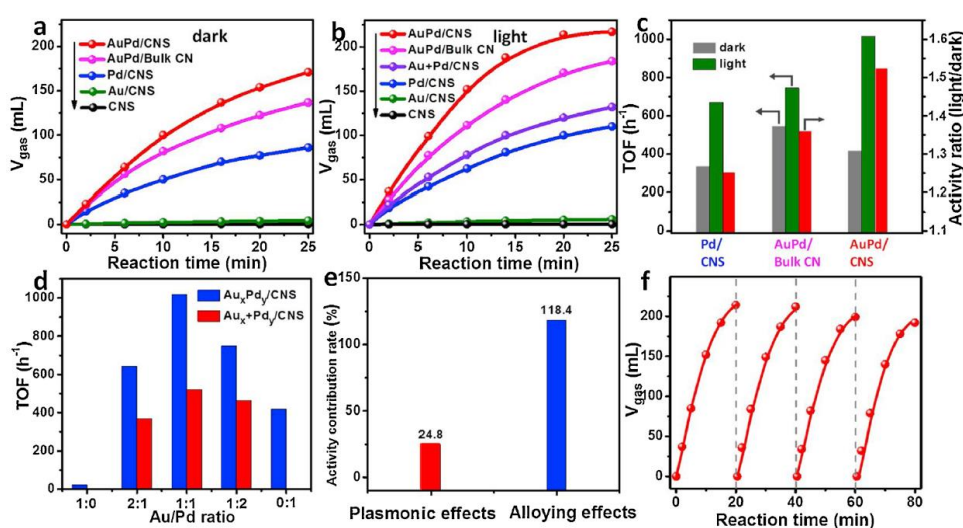
Figure 11. Time-dependent gas (H_2 and CO_2) evolution curves from formic acid of all the as-prepared materials (a) in the dark at 25 °C and (b) under visible light irradiation (λ > 420 nm) at 25 °C. (c) The TOFs and activity ratio of different catalysts in the dark and under visible light irradiation [TOF was calculated from the data within the first 10 min according to the following equation: TOF = mmol gas produced/(mmolAuPd × h)]. (d) The TOFs of Au_xPd_y/CNS and Au_x+Pd_y/CNS under visible light irradiation. (e) The activity contribution rate of alloying effects and plasmonic effects under visible light irradiation. (f) The recycling performance of AuPd/CNS under visible light irradiation (λ > 420 nm). Reprinted with permission from [52].

Furthermore, the reaction mechanism summarized in Figure 12 was also proposed in that study. In dark condition, FA is auto-oxidized and the reduction to H_2 and CO_2 takes place on the Pd active sites of the alloy system by means of thermal power. Under visible-light irradiation conditions, electron-electron collisions and electron distribution between Au and Pd happen because of the alloying and plasmonic effects. Furthermore, the photogenerated electron of CNS transfer to Pd sites, leading to the formation of electron-rich Pd species. FA is oxidized to form CO_2 and H^+ by the holes on CNS and such H^+ are reduced to H_2 by the electron-rich Pd species.
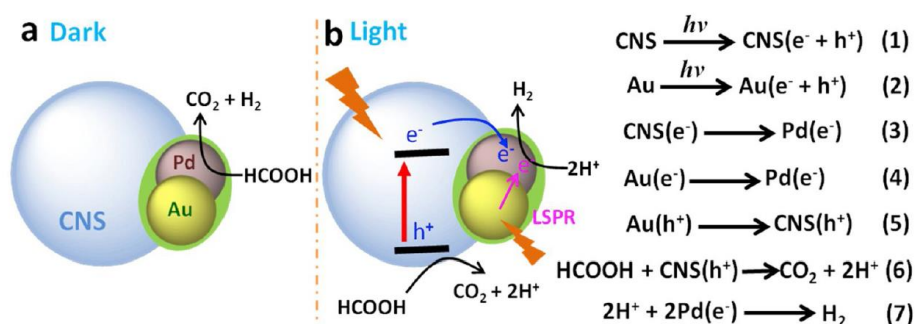
Figure 12. Schematic illustration of photocatalytic hydrogen evolution from formic acid for AuPd/CNS (a) under dark and (b) light. Reprinted with permission from [52].

5. Other photocatalytic systems

Aside from the most commonly photocatalytic systems based on TiO_2, CdS, and C_3N_4, some other nice works aiming at catalysing the photodecomposition of FA have also been reported in the recent literature.

For instance, Tabata et al. investigated the use of silicon-base material for the production of H_2 under visible-light irradiation [107]. Pure Si powder and metal-containing catalysts (Pt, Pd, or Ru) were evaluated. In that case, the catalytic ability was shown to follow the order Ru/Si > Pd/Si > Pt/Si > Si.

Moskovits et al. prepared a series of Pd nanostructures to serve as plasmon-mediated photocatalytic for the decomposition of FA [108]. The investigated nanostructures were nanocubes (average edge length of 10 nm) and hexagonal nanosheets (average edge lengths of 22 nm and thickness of 2.9 nm) with the same surface-to-volume ratio.

Kakuta and Abe reported on the utilization of Cu_2O and $Pt-Cu_2O$ as visible-light-responsive photocatalysts to boost the decomposition of FA [109]. According to the valence and conduction band edge of Cu_2O (+0.844 V and -1.16 V, vs SHE (pH 7), respectively), it was determined that the oxidation of FA ($HCOOH + 2h^+ \rightarrow CO_2 + 2H^+$) and the generation of H_2 was feasible ($2h^+ + 2e^- \rightarrow H_2$). The catalytic test under dark condition did not produce gas, indicating that, using such system, the decomposition of FA takes place *via* photocatalytic process. Upon irradiation, the production of H_2 with both Cu_2O and $Pt-Cu_2O$ showed a linear trend with the irradiation time, and it was larger for $Pt-Cu_2O$. That study was claimed to be the first instance in reporting the selective and stoichiometric decomposition of FA to H_2 and CO_2 with a visible-light-responsive photocatalyst.

Wang et. al recently reported on Pt Single Atoms on Te nanowires (Te NWs) for plasmon-enhanced dehydrogenation of FA [110]. Initially, Te NWs were prepared from Na_2TeO_3 and they were loaded with Pt contents of 1.1, 4.6, and 32.0 wt.%, so as to result in the formation of Pt single atoms, nanoclusters and nanocrystals (average size of ~4 nm), 1.1%Pt/Te, 4.6%Pt/Te, and 32.0%Pt/Te, respectively. Furthermore, a commercial Pt/C sample with an average nanoparticle size of ~ 4-5 nm was also assessed. The reaction tests revealed that, while the decomposition of FA was almost negligible under dark conditions, the performance was greatly enhanced under light irradiation, reaching TOF values of TOFs 3070, 1205, 580, and 363 h^{-1} for 1.1%Pt/Te, 4.6%Pt/Te, 32.0%Pt/Te, and Pt/C under, respectively. In addition, the photocatalysts were evaluated under various light wavelengths. It was observed that in the case of 1.1%Pt/Te, 4.6%Pt/Te the apparent quantum efficiency (AQE) irradiated by light with different wavelength followed the same tendency as the UV–vis spectrum, being such tendency deviated for the sample with the highest Pt content. Additional tests were conducted to elucidate the plasmonic electron-driven mechanism and photothermal effect accompanied by plasmonic effect factors. The linear dependence of TOFs values with the light intensity observed for 1.1%Pt/Te confirmed the importance of the plasmonic electron-driven mechanism for the photocatalysts with low Pt content, while the photothermal effect gains importance for higher Pt content.

Su et al. reported on the visible-light-driven catalytic activity enhancement of Pd in AuPd nanoparticles supported on graphene oxide (AuPd/GO) [111]. As previously mentioned for some other bimetallic AuPd systems discussed above, the significant effect of the electron transfer from Au to Pd was claimed to be crucial for the enhancement achieved by the AuPd-system under visible-light irradiation. Wen et al. also reported on AuPd-based photocatalysts for the decomposition of FA by using a more sophisticated

photocatalyst formed by plasmonic Au@Pd nanoparticles supported on titanium-doped zirconium-based amine functionalized metal−organic frameworks (MOFs) (UiO-66(Zr$_{100-x}$Ti$_x$)) [112]. It was observed that the integration of the components of the catalyst resulted in a highly effective light energy harvesting system able to catalyze the dehydrogenation of FA under visible-light irradiation without any additive.

As for the case of thermal catalysts used in the FA decomposition [47, 49] , the beneficial role of N-doped materials in achieved enhanced performances has also been indicated for photocatalytic processes. In this line, the photocatalytic activity of N-doped carbon quantum dots (NCQDs) in the production of H$_2$ from FA was evaluated by Li et al. [113]. In that study, NCQDs of average diameter of 2.5 nm were obtained from the waste of shrimp by hydrothermal treatment and washing and their photoactivity was evaluated using external sunlight irradiation.

As can be seen from the results summarized in these sections, there are diverse strategies considered for the preparation of photocatalytic systems used in the photodecomposition of FA. In order to give the readers a comparison of the performance achieved, the results of some representative photocatalysts are listed in Table 1.

Table 1. Comparison of the performance of various photocatalytic systems in the conversion of FA to H$_2$.

Photocatalyst	Production of H$_2$ [mmol H$_2$ g catalyst $^{-1}$ h $^{-1}$]	Selectivity to H$_2$	Light	Reference
TiO$_2$ nanofibers	0.80	69.6	AM1.5, 1 sun	[81]
Pd-TiO$_2$ nanofibers	10.9	98.2	AM1.5, 1 sun	[81]
Au-TiO$_2$ nanofibers	3.9	90.7	AM1.5, 1 sun	[81]
AuPd-TiO$_2$ nanofibers	17.7	99.7	AM1.5, 1 sun	[81]
Pt-TiO$_2$	1.62	n/a	UV	[114]
Cu-TiO$_2$	0.83	n/a	UV	[115]

Rh-N-TiO$_2$	0.75	98	230-440 nm	[116]
Bulk CdS	0.08	n/a	>400 nm	[86]
Pt-CdS	0.85	83	>400 nm	[117]
CdS nanorods	0.22	n/a	>420 nm	[118]
Pt-CdS nanorods	4.46	n/a	>420 nm	[118]
Pt-CdS-TNT	4.26	n/a	>420 nm	[88]
CdS-TNT + WO3	0.62	n/a	>420 nm	[88]
Pt-CdS-QD	1.22	n/a	>420 nm	[119]
CdS@Al-HMS	0.13	n/a	>420 nm	[120]
Ru-CdS@Al-HMS	0.54	n/a	>420 nm	[120]
CdS/ZnS nanoparticles	1.24	n/a	>420 nm	[90]
Ru-CdS/ZnS nanoparticles	5.85	n/a	>420 nm	[90]
Pd@C$_3$N$_4$	53.4	100	>400 nm	[105]

6. Conclusion and outlook

In the present review the promising role of hydrogen as an energy vector able to replace the widely used vectors based on fossil fuels is pointed out. Furthermore, the suitability of FA as a Liquid Organic Hydrogen Carrier (LOHC) is highlighted by summarizing its features and some of the most representative studies aiming at reporting on the photocatalytic decomposition of FA are herein summarized. In order to consider the most widely investigated photocatalytic systems studies for the present application, sections on TiO$_2$, CdS and C$_3$N$_4$-based photocatalysts have been included in this manuscript. Along these sections, it has been evidenced that, as in the case of the thermal decomposition of FA, the addition of metal nanoparticles is vital to accelerate the photocatalytic process. In this line, Mott–Schottky photocatalysts have shown to be a very promising approach to adjust the surface charge density of the active metal phase, while decreasing the recombination of electron-holes pairs by transferring of the photogenerated electrons from the semiconductor supports to the metal active phase. Such electron-rich metal

species are, in turn, more active to boost the hydrogen production from FA. This is particularly important for the Pd-based catalysts. Moreover, it has been observed that the utilization of alloy nanoparticles further promotes the formation of electron-rich Pd species. In addition, the incorporation of agent to control the size and shape of the nanoparticles are a useful resource to afford optimized performances. Particular attention has been paid to those systems containing plasmonic nanoparticles (PdAg and PdAu).

Aside from noble metal-containing photocatalysts, noble-metal-free systems have also been studied in this application. For instance, the utilization of heterojunction (i.e. CuO/TiO_2, CdS/Fe_2O_3, MoS_2/CdS, etc.) or core-shell structures (i.e. CdS@ZIF-8, CdS-ZnS, etc.) has been shown to afford enhanced performances ascribed to efficient electron-hole pairs separation at the interface. Such systems are also promising from the economic viewpoint. Furthermore, the importance of some other photocatalytic systems (i.e. MOFs, GO, NCQDs, etc.) has also been briefly mentioned.

This review highlights the applicability of photocatalyst in the hydrogen production from LOHC. It is expected to provide the readership with an overview of the most representative approaches utilized so far for this application at the time that aims at encouraging the research community to further explore on the exciting and relatively hardly investigated photocatalytic decomposition of formic acid. Even though important breakthroughs have recently been achieved in the photodecomposition of FA, the materials used until now are far to be as sophisticated as those used for some other traditional photocatalytic applications. It could be envisaged that such important application will soon deserve new efforts towards the design of efficient photocatalytic systems. One of the points to be considered in this respect would be the improvement of the stability of the photocatalysts, which has been shown to be lacking until now. Such aspect could be enhanced by engineering the optical properties of the materials used as

well as by controlling the adsorption of the reaction intermediates, which would eventually block the active sites. Furthermore, another point to be considered would be the development of photocatalysts with higher surface area able to provide a higher dispersion of the active sites. In this line, the combination of the traditionally used photocatalytic materials (i.e. TiO_2, CdS, g-C_3N_4) with a second component with a higher developed porosity (i.e. carbon materials, etc.) could be a resourceful alternative to afford highly efficient systems for the photodecomposition of FA.

References

1. Kothandaraman J, Kar S, Sen R, et al (2017) Efficient Reversible Hydrogen Carrier System Based on Amine Reforming of Methanol. J Am Chem Soc 139:2549–2552.

2. https://www.epa.gov/ghgemissions/understanding-global-warming-potentials

3. Pires JCM (2019) Negative emissions technologies: A complementary solution for climate change mitigation. Sci Total Environ 672:502–514.

4. http://unfccc.int/paris_agreement/items/9485.php

5. Markiewicz M, Zhang YQ, Bösmann A, et al (2015) Environmental and health

impact assessment of Liquid Organic Hydrogen Carrier (LOHC) systems – challenges and preliminary results. Energy Environ Sci 8:1035–1045.

6.   Gahleitner G (2013) Hydrogen from renewable electricity: An international review of power-to-gas pilot plants for stationary applications. Int J Hydrogen Energy 38:2039–2061.

7.   Kousksou T, Bruel P, Jamil A, et al (2014) Energy storage: Applications and challenges. Sol Energy Mater Sol Cells 120:59–80.

8.   https://www.iea.org/publications/freepublications/publication/
      TechnologyRoadmapHydrogenandFuelCells.pdf

9.   Aakko-Saksa PT, Cook C, Kiviaho J, Repo T (2018) Liquid organic hydrogen carriers for transportation and storing of renewable energy – Review and discussion. J Power Sources 396:803–823.

10.   Dincer I, Acar C (2015) Review and evaluation of hydrogen production methods for better sustainability. Int J Hydrogen Energy 40:11094–11111.

11.   Niermann M, Drünert S, Kaltschmitt M, Bonhoff K (2019) Liquid organic hydrogen carriers (LOHCs) – techno-economic analysis of LOHCs in a defined process chain. Energy Environ Sci 12:290–307.

12.   Rigas F, Sklavounos S (2005) Evaluation of hazards associated with hydrogen storage facilities. Int J Hydrogen Energy 30:1501–1510.

13.   Edwards PP, Kuznetsov VL, David WIF, Brandon NP (2008) Hydrogen and fuel cells: Towards a sustainable energy future. Energy Policy 36:4356–4362.

14.   Zheng J, Liu X, Xu P, et al (2012) Development of high pressure gaseous hydrogen

storage technologies. Int J Hydrogen Energy 37:1048–1057.

15.   Dadashzadeh M, Kashkarov S, Makarov D, Molkov V (2018) Risk assessment methodology for onboard hydrogen storage. Int J Hydrogen Energy 43:6462–6475.

16.   Lillo-Ródenas MA, Guo ZX, Aguey-Zinsou KF, et al (2008) Effects of different carbon materials on MgH_2 decomposition. 46:126–137.

17.   Shi J, Kuwahara Y, Wen M, et al (2016) Room-Temperature and Aqueous-Phase Synthesis of Plasmonic Molybdenum Oxide Nanoparticles for Visible-Light-Enhanced Hydrogen Generation. Chem – An Asian J 11:2377–2381.

18.   Salinas-Torres D, Navlani-García M, Kuwahara Y, et al (2019) Non-noble metal doped perovskite as a promising catalyst for ammonia borane dehydrogenation. Catal Today. https://doi.org/10.1016/j.cattod.2019.03.072

19.   García-Aguilar J, Navlani-García M, Berenguer-Murcia Á, et al (2016) Enhanced ammonia-borane decomposition by synergistic catalysis using CoPd nanoparticles supported on titano-silicates. RSC Adv 6:91768–91772.

20.   Navlani-garcía M, Verma P, Kuwahara Y, et al (2018) Visible-light-enhanced catalytic activity of Ru nanoparticles over. J Photochem Photobiol A 358:327–333.

21.   Fuku K, Kamegawa T, Mori K, Yamashita H (2012) Highly Dispersed Platinum Nanoparticles on TiO_2 Prepared by Using the Microwave-Assisted Deposition Method: An Efficient Photocatalyst for the Formation of H_2 and N_2 from Aqueous NH_3. Chem - An Asian J 7:1366–1371.

22.   Lan R, Irvine JTS, Tao S (2012) Ammonia and related chemicals as potential indirect hydrogen storage materials. Int J Hydrogen Energy 37:1482–1494.

23.   Afif A, Radenahmad N, Cheok Q, et al (2016) Ammonia-fed fuel cells: A

comprehensive review. Renew Sustain Energy Rev 60:822–835.

24.   Chowdhury AD, Agnihotri N, De A (2015) Hydrolysis of sodium borohydride using Ru-Co-PEDOT nanocomposites as catalyst. Chem Eng J 264:531–537.

25.   Dalebrook AF, Gan W, Grasemann M, et al (2013) Hydrogen storage: beyond conventional methods. Chem Commun 49:8735–8751.

26.   Preuster P, Papp C, Wasserscheid P (2017) Liquid Organic Hydrogen Carriers (LOHCs): Toward a Hydrogen-free Hydrogen Economy. Acc Chem Res 50:74–85.

27.   Niermann M, Beckendorff A, Kaltschmitt M, Bonhoff K (2019) Liquid Organic Hydrogen Carrier (LOHC) – Assessment based on chemical and economic properties. Int J Hydrogen Energy 44:6631–6654.

28.   Hu P, Fogler E, Diskin-Posner Y, et al (2015) A novel liquid organic hydrogen carrier system based on catalytic peptide formation and hydrogenation. Nat Commun 6:6859.

29.   Mori K, Dojo M, Yamashita H (2013) Pd and Pd-Ag nanoparticles within a macroreticular basic resin: An efficient catalyst for hydrogen production from formic acid decomposition. ACS Catal 3:1114–1119.

30.   Navlani-García M, Mori K, Kuwahara Y, Yamashita H (2018) Recent strategies targeting efficient hydrogen production from chemical hydrogen storage materials over carbon-supported catalysts. NPG Asia Mater 1–16.

31.   Navlani-García M, Mori K, Salinas-Torres D, et al (2019) New Approaches Toward the Hydrogen Production From Formic Acid Dehydrogenation Over Pd-Based Heterogeneous Catalysts. Front Mater 6:44.

32. García-Aguilar J, Navlani-García M, Berenguer-Murcia Á, et al (2016) Evolution of the PVP-Pd surface interaction in nanoparticles through the case study of formic acid decomposition. Langmuir 32:12110–12118.

33. Podyacheva OY, Bulushev DA, Suboch AN, et al (2018) Highly Stable Single-Atom Catalyst with Ionic Pd Active Sites Supported on N-Doped Carbon Nanotubes for Formic Acid Decomposition. ChemSusChem 11:3724–3727.

34. Bulushev DA, Zacharska M, Shlyakhova E V, et al (2016) Single Isolated Pd^{2+} Cations Supported on N-Doped Carbon as Active Sites for Hydrogen Production from Formic Acid Decomposition. ACS Catal 6:681–691.

35. Bulushev DA, Bulusheva LG, Beloshapkin S, et al (2015) Pd clusters supported on amorphous, low-porosity carbon spheres for hydrogen production from formic acid. ACS Appl Mater Interfaces 7:8719–8726.

36. Mellmann D, Sponholz P, Junge H, Beller M (2016) Formic acid as a hydrogen storage material-development of homogeneous catalysts for selective hydrogen release. Chem Soc Rev 45:3954–3988.

37. Enthaler S, Von Langermann J, Schmidt T (2010) Carbon dioxide and formic acid - The couple for environmental-friendly hydrogen storage? Energy Environ Sci 3:1207–1217.

38. Coffey RS (1967) The decomposition of formic acid catalysed by soluble metal complexes. Chem Commun 1967: 923–924.

39. Fellay C, Dyson PJ, Laurenczy G (2008) A viable hydrogen-storage system based on selective formic acid decomposition with a ruthenium catalyst. Angew Chemie - Int Ed 47:3966–3968.

40. Loges B, Boddien A, Junge H, Beller M (2008) Controlled generation of hydrogen from formic acid amine adducts at room temperature and application in H_2/O_2 fuel cells. Angew Chemie - Int Ed 47:3962–3965.

41. Iglesias M, Oro LA (2018) Mechanistic Considerations on Homogeneously Catalyzed Formic Acid Dehydrogenation. Eur J Inorg Chem 2018:2125–2138.

42. Navlani-García M, Mori K, Nozaki A, et al (2016) Investigation of Size Sensitivity in the Hydrogen Production from Formic Acid over Carbon-Supported Pd Nanoparticles. ChemistrySelect 1:1879–1886.

43. Navlani-García M, Mori K, Nozaki A, et al (2016) Screening of Carbon-Supported PdAg Nanoparticles in the Hydrogen Production from Formic Acid. Ind Eng Chem Res 55:7612–7620.

44. Navlani-García M, Salinas-Torres D, Mori K, et al (2018) Enhanced formic acid dehydrogenation by the synergistic alloying effect of PdCo catalysts supported on graphitic carbon nitride. Int. J. Hydrogen Energy. https://doi.org/10.1016/j.ijhydene.2018.11.057

45. Sun J, Qiu H, Cao W, et al (2019) Ultrafine Pd Particles Embedded in Nitrogen-Enriched Mesoporous Carbon for Efficient H_2 Production from Formic Acid Decomposition. ACS Sustain Chem Eng 7:1963–1972.

46. Mori K, Sano T, Kobayashi H, Yamashita H (2018) Surface Engineering of a Supported PdAg Catalyst for Hydrogenation of CO_2 to Formic Acid: Elucidating the Active Pd Atoms in Alloy Nanoparticles. J Am Chem Soc 140:8902–8909.

47. Salinas-Torres D, Navlani-García M, Mori K, et al (2019) Nitrogen-doped carbon materials as a promising platform toward the efficient catalysis for hydrogen

generation. Appl Catal A Gen 571:25–41.

48.   Navlani-García M, Martis M, Lozano-Castelló D, et al (2015) Investigation of Pd nanoparticles supported on zeolites for hydrogen production from formic acid dehydrogenation. Catal Sci Technol 5:364–371.

49.   Navlani-García M, Salinas-Torres D, Mori K, et al (2019) Insights on palladium decorated nitrogen-doped carbon xerogels for the hydrogen production from formic acid. Catal Today 324:90–96.

50.   Wu Y, Wen M, Navlani-García M, et al (2017) Palladium nanoparticles supported on titanium doped graphitic carbon nitride for formic acid dehydrogenation. Chem - An Asian J 12:860–867.

51.   Navlani-García M, Miguel-García I, Berenguer-Murcia Á, et al (2016) Pd/zeolite-based catalysts for the preferential CO oxidation reaction: Ion-exchange, Si/Al and structure effect. 6:2623–2632.

52.   Zhang S, Li M, Zhao J, et al (2019) Plasmonic AuPd-based Mott-Schottky photocatalyst for synergistically enhanced hydrogen evolution from formic acid and aldehyde. Appl Catal B Environ 252:24–32.

53.   Kim JH, Hansora D, Sharma P, et al (2019) Toward practical solar hydrogen production – an artificial photosynthetic leaf-to-farm challenge. Chem Soc Rev 48:1908–1971.

54.   Takata T, Domen K (2019) Particulate Photocatalysts for Water Splitting: Recent Advances and Future Prospects. ACS Energy Lett 4:542–549.

55.   Murdoch, Waterhouse, Nadeem, et al (2010) Photocatalytic hydrogen production from ethanol over Au/TiO$_2$ anatase and rutile nanoparticles: Effect of Au particle

size. ACS Natl Meet B Abstr 3:1.

56. Gallo A, Marelli M, Psaro R, et al (2012) Bimetallic Au–Pt/TiO$_2$ photocatalysts active under UV-A and simulated sunlight for H$_2$ production from ethanol. Green Chem 14:330–333.

57. Wu N-L, Lee M-S (2004) Enhanced TiO$_2$ photocatalysis by Cu in hydrogen production from aqueous methanol solution. Int J Hydrogen Energy 29:1601–1605.

58. Jing D, Guo L (2007) Hydrogen production over Fe-doped tantalum oxide from an aqueous methanol solution under the light irradiation. J Phys Chem Solids 68:2363–2369.

59. Montini T, Monai M, Beltram A, et al (2016) H$_2$ production by photocatalytic reforming of oxygenated compounds using TiO$_2$-based materials. Mater Sci Semicond Process 42:122–130.

60. de Oliveira Melo M, Silva LA (2011) Visible light-induced hydrogen production from glycerol aqueous solution on hybrid Pt–CdS–TiO$_2$ photocatalysts. J Photochem Photobiol A Chem 226:36–41.

61. Jana MK, Gupta U, Rao CNR (2016) Hydrazine as a hydrogen carrier in the photocatalytic generation of H2 using CdS quantum dots. Dalt Trans 45:15137–15141.

62. Yuzawa H, Mori T, Itoh H, Yoshida H (2012) Reaction Mechanism of Ammonia Decomposition to Nitrogen and Hydrogen over Metal Loaded Titanium Oxide Photocatalyst. J Phys Chem C 116:4126–4136.

63. Reli M, Ambrožová N, Šihor M, et al (2015) Novel cerium doped titania catalysts

for photocatalytic decomposition of ammonia. Appl Catal B Environ 178:108–116.

64. Navlani-garcía M, Verma P, Kuwahara Y, Kamegawa T (2018) Visible-light-enhanced catalytic activity of Ru nanoparticles over carbon modified g-C_3N_4. J Photochem Photobiol A 358:327–333.

65. Liu P-H, Wen M, Tan C-S, et al (2017) Surface plasmon resonance enhancement of production of H_2 from ammonia borane solution with tunable Cu_2−xS nanowires decorated by Pd nanoparticles. Nano Energy 31:57–63.

66. Verma P, Yuan K, Kuwahara Y, et al (2018) Enhancement of plasmonic activity by Pt/Ag bimetallic nanocatalyst supported on mesoporous silica in the hydrogen production from hydrogen storage material. Appl Catal B Environ 223:10–15.

67. Ji Y, Luo Y (2016) Structure-dependent photocatalytic decomposition of formic acid on the anatase TiO_2(101) surface and strategies to increase its reaction rate. J Power Sources 306:208–212.

68. Civiš S, Ferus M, Zukalová M, et al (2012) Photochemistry and gas-phase FTIR spectroscopy of formic acid interaction with anatase $Ti_{18}O_2$ nanoparticles. J Phys Chem C 116:11200–11205.

69. Liu S, Yu J, Jaroniec M (2011) Anatase TiO_2 with Dominant High-Energy {001} Facets: Synthesis, Properties, and Applications. Chem Mater 23:4085–4093.

70. Roy P, Berger S, Schmuki P (2011) TiO_2 Nanotubes: Synthesis and Applications. Angew Chemie Int Ed 50:2904–2939.

71. Fujishima A, Honda K (1972) Electrochemical Photolysis of Water at a Semiconductor Electrode. Nature 238:37–38.

72. Fujishima A, Zhang X (2006) Titanium dioxide photocatalysis: present situation

and future approaches. Comptes Rendus Chim 9:750–760.

73. Kumaravel V, Mathew S, Bartlett J, Pillai SC (2019) Photocatalytic hydrogen production using metal doped TiO_2: A review of recent advances. Appl Catal B Environ 244:1021–1064.

74. Ma D, Liu A, Li S, et al (2018) TiO_2 photocatalysis for C–C bond formation. Catal Sci Technol 8:2030–2045.

75. Fernández-Catalá J, Cazorla-Amorós D, Berenguer-Murcia Á (2018) Facile encapsulation of P25 (TiO_2) in spherical silica with hierarchical porosity with enhanced photocatalytic properties for gas-phase propene oxidation. Appl Catal A Gen 564:123–132.

76. Cano-Casanova L, Amorós-Pérez A, Ouzzine M, et al (2018) One step hydrothermal synthesis of TiO_2 with variable HCl concentration: Detailed characterization and photocatalytic activity in propene oxidation. Appl Catal B Environ 220:645–653.

77. Amorós-Pérez A, Cano-Casanova L, Lillo-Ródenas MÁ, Román-Martínez MC (2017) Cu/TiO_2 photocatalysts for the conversion of acetic acid into biogas and hydrogen. Catal Today 287:78–84.

78. Song R, Luo B, Liu M, et al (2017) Synergetic coupling of photo and thermal energy for efficient hydrogen production by formic acid reforming. AIChE J 63:2916–2925.

79. Liu P, Cai Z, You Y, et al (2018) Surface Modification on Pd-TiO2 Hybrid Nanostructures towards Highly Efficient H_2 Production from Catalytic Formic Acid Decomposition. Chem – A Eur J 24:18398–18402.

80. Tsuji M, Shimamoto D, Uto K, et al (2016) Enhancement of catalytic activity of AgPd@Pd/TiO$_2$ nanoparticles under UV and visible photoirradiation. J Mater Chem A 4:14649–14656.

81. Zhang Z, Cao S, Liao Y, Xue C (2015) Selective photocatalytic decomposition of formic acid over AuPd nanoparticle-decorated TiO$_2$ nanofibers toward high-yield hydrogen production. Appl Catal B, Environ 162:204–209.

82. Wu M, Zhang M, Lv T, et al (2017) The effect of calcination atmosphere upon the photocatalytic performance of Au-La$_2$O$_3$/TiO$_2$ for hydrogen production from formic acid. Appl Catal A Gen 547:96–104.

83. Zhang Z, Liu K, Bao Y, Dong B (2017) Photo-assisted self-optimizing of charge-carriers transport channel in the recrystallized multi-heterojunction nanofibers for highly efficient photocatalytic H$_2$ generation. Appl Catal B Environ 203:599–606.

84. Li Q, Li X, Wageh S, et al (2015) CdS/Graphene Nanocomposite Photocatalysts. Adv Energy Mater 5:1500010.

85. Tada H, Naya S-I, Fujishima M (2018) Water splitting by plasmonic photocatalysts with a gold nanoparticle/cadmium sulfide heteroepitaxial junction: A mini review. Electrochem commun 97:22–26.

86. Willner I, Goren Z (1986) Photodecomposition of formic acid by cadmium sulphide semiconductor particles. J Chem Soc Chem Commun 172–173.

87. Nedoluzhko AI, Shumilin IA, Nikandrov V V (1996) Coupled Action of Cadmium Metal and Hydrogenase in Formate Photodecomposition Sensitized by CdS. J Phys Chem 100:17544–17550.

88. Yeh HM, Lo SL, Chen MJ, Chen HY (2014) Hydrogen production from formic

acid solution by modified TiO_2 and titanate nanotubes in a two-step system under visible light irradiation. Water Sci Technol 69:1676–1681.

89.　Chen H-Y, Lo S-L, Lai Y-C, Liou Y-H (2018) Titanate nanotubes coupled with Pt nanoparticles for the inhibition of CdS photocorrosion during visible-light-driven hydrogen production from formic acid. Mater Res Express 5:9.

90.　Wang X, Peng W-C, Li X-Y (2014) Photocatalytic hydrogen generation with simultaneous organic degradation by composite CdS-ZnS nanoparticles under visible light. Int J Hydrogen Energy 39:13454–13461.

91.　Zeng M, Chai Z, Deng X, et al (2016) Core–shell CdS@ZIF-8 structures for improved selectivity in photocatalytic H_2 generation from formic acid. Nano Res 9:2729–2734.

92.　Zhang YJ, Zhang L (2009) Preparation of Ru-loaded CdS/Al-HMS nanocomposites and production of hydrogen by photocatalytic degradation of formic acid. Appl Surf Sci 255:4863–4866.

93.　Kuehnel MF, Wakerley DW, Orchard KL, Reisner E (2015) Photocatalytic Formic Acid Conversion on CdS Nanocrystals with Controllable Selectivity for H_2 or CO. Angew Chemie - Int Ed 54:9627–9631.

94.　Cao S, Chen Y, Wang H, et al (2018) Ultrasmall CoP Nanoparticles as Efficient Cocatalysts for Photocatalytic Formic Acid Dehydrogenation. Joule 2:549–557.

95.　Nasir JA, Hafeez M, Arshad M, et al (2018) Photocatalytic Dehydrogenation of Formic Acid on CdS Nanorods through Ni and Co Redox Mediation under Mild Conditions. ChemSusChem 11:2587–2592.

96.　Dong F, Zhao Z, Xiong T, et al (2013) In Situ Construction of g-C_3N_4/g-C_3N_4

Metal-Free Heterojunction for Enhanced Visible-Light Photocatalysis. ACS Appl Mater Interfaces 5:11392–11401.

97.   Huang H, Yang S, Vajtai R, et al (2014) Pt-Decorated 3D Architectures Built from Graphene and Graphitic Carbon Nitride Nanosheets as Efficient Methanol Oxidation Catalysts. Adv Mater 26:5160–5165.

98.   Ong W-J, Tan L-L, Ng YH, et al (2016) Graphitic Carbon Nitride (g-C_3N_4)-Based Photocatalysts for Artificial Photosynthesis and Environmental Remediation: Are We a Step Closer To Achieving Sustainability? Chem Rev 116:7159–7329.

99.   Goettmann F, Fischer A, Antonietti M, Thomas A (2006) Metal-free catalysis of sustainable Friedel–Crafts reactions: direct activation of benzene by carbon nitrides to avoid the use of metal chlorides and halogenated compounds. Chem Commun 4530–4532.

100.   Wang X, Maeda K, Thomas A, et al (2009) A metal-free polymeric photocatalyst for hydrogen production from water under visible light. Nat Mater 8:76–80.

101.   Fu J, Yu J, Jiang C, Cheng B (2018) g-C_3N_4-Based Heterostructured Photocatalysts. Adv Energy Mater 8:1701503.

102.   Mamba G, Mishra AK (2016) Graphitic carbon nitride (g-C_3N_4) nanocomposites: A new and exciting generation of visible light driven photocatalysts for environmental pollution remediation. Appl Catal B Environ 198:347–377.

103.   Fajrina N, Tahir M (2019) A critical review in strategies to improve photocatalytic water splitting towards hydrogen production. Int J Hydrogen Energy 44:540–577.

104.   Xiao L, Jun Y-S, Wu B, et al (2017) Carbon nitride supported AgPd alloy nanocatalysts for dehydrogenation of formic acid under visible light. J Mater Chem

A 5:6382–6387.

105. Photocatalyst NMS, Cai Y, Li X, et al (2013) Highly Efficient Dehydrogenation of Formic Acid over a Palladium- Angewandte. Angew Chemie 125:1–5.

106. Liu H, Liu X, Yang W, et al (2019) Photocatalytic dehydrogenation of formic acid promoted by a superior PdAg@g-C$_3$N$_4$ Mott–Schottky heterojunction. J Mater Chem A.

107. Tsutsumi K, Kashimura N, Tabata K (2015) Photo-Assisted Hydrogen Evolution in Aqueous Solution of Formic Acid with Silicon which is Supported with Noble Metals. Silicon 7:43–48.

108. Wu B, Lee J, Mubeen S, et al (2016) Plasmon-Mediated Photocatalytic Decomposition of Formic Acid on Palladium Nanostructures. 4:1041–1046.

109. Kakuta S, Abe T (2009) A Novel Example of Molecular Hydrogen Generation from Formic Acid at Visible-Light-Responsive Photocatalyst. ACS Appl Mater Interfaces 1:2707–2710.

110. Han L, Zhang L, Wu H, et al (2019) Anchoring Pt Single Atoms on Te Nanowires for Plasmon-Enhanced Dehydrogenation of Formic Acid at Room Temperature. Adv Sci. https://doi.org/10.1002/advs.201900006

111. Liu P, Gu X, Zhang H, et al (2017) Visible-light-driven catalytic activity enhancement of Pd in AuPd nanoparticles for hydrogen evolution from formic acid at room temperature. Appl Catal B Environ 204:497–504.

112. Wen M, Mori K, Kuwahara Y, Yamashita H (2017) Plasmonic Au@Pd nanoparticles supported on a basic metal-organic framework: Synergic boosting of H2production from formic acid. ACS Energy Lett 2:1–7.

113. Wei J, Wang H, Zhang Q, Li Y (2015) One-pot hydrothermal synthesis of N-Doped carbon quantum dots using the waste of shrimp for hydrogen evolution from formic acid. Chem Lett 44:241–243.

114. Li Y, He F, Peng S, et al (2011) Effects of electrolyte NaCl on photocatalytic hydrogen evolution in the presence of electron donors over Pt/TiO$_2$. J Mol Catal A Chem 341:71–76.

115. Lanese V, Spasiano D, Marotta R, et al (2013) Hydrogen production by photoreforming of formic acid in aqueous copper/TiO$_2$ suspensions under UV-simulated solar radiation at room temperature. Int J Hydrogen Energy 38:9644–9654.

116. Halasi G, Schubert G, Solymosi F (2012) Photolysis of HCOOH over Rh deposited on pure and N-modified TiO$_2$: Production of pure H$_2$. Catal Letters 142:218–223.

117. Matsumura M, Hiramoto M, Iehara T, Tsubomura H (1984) Photocatalytic and photoelectrochemical reactions of aqueous solutions of formic acid, formaldehyde, and methanol on platinized CdS powder and at a CdS electrode. J Phys Chem 88:248–250

118. Li Y, Hu Y, Peng S, et al (2009) Synthesis of CdS nanorods by an ethylenediamine assisted hydrothermal method for photocatalytic hydrogen evolution. J Phys Chem C 113:9352–9358.

119. Li Y, Tang L, Peng S, et al (2012) Phosphate-assisted hydrothermal synthesis of hexagonal CdS for efficient photocatalytic hydrogen evolution. CrystEngComm 14:6974–6982.

120. Zhang YJ, Zhang L, Li S (2010) Synthesis of Al-substituted mesoporous silica

coupled with CdS nanoparticles for photocatalytic generation of hydrogen. Int J

Hydrogen Energy 35:438–444.